Cell Reports

Article

Dendrite architecture determines mitochondrial distribution patterns *in vivo*

Graphical abstract

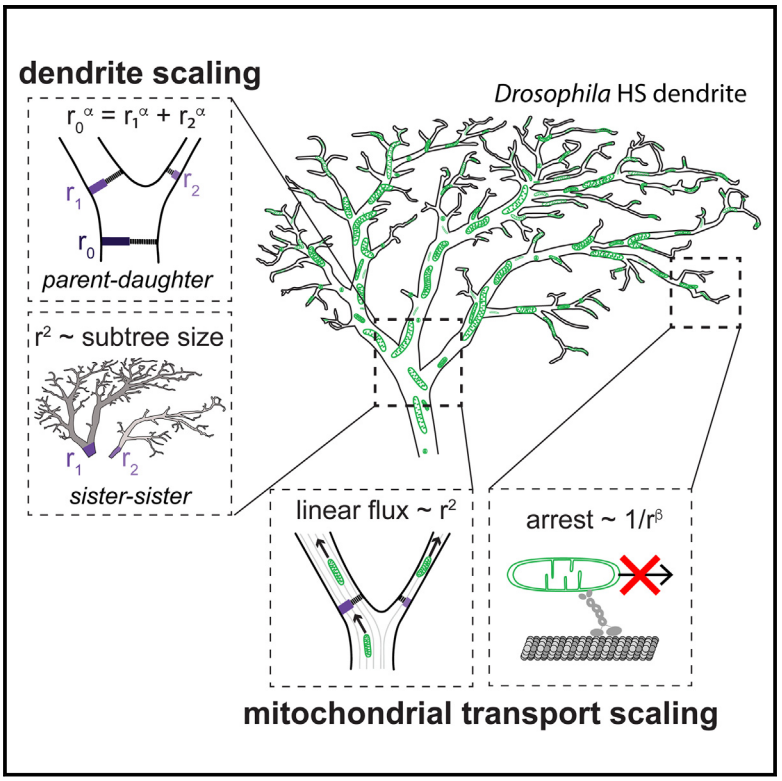

Highlights

- A model for transport in dendrites predicts global mitochondrial localization patterns
- In this model, specific scaling rules recapitulate realistic mitochondrial distributions
- *Drosophila* HS dendrites obey these specific scaling rules

Authors

Eavan J. Donovan, Anamika Agrawal, Nicole Liberman, ..., Nicholas J. Chua, Elena F. Koslover, Erin L. Barnhart

Correspondence

eb3305@columbia.edu

In brief

Donovan et al. combine mathematical modeling with *in vivo* measurements of mitochondrial transport and neuronal architecture in *Drosophila* HS (horizontal system) neurons to demonstrate that global, steady-state mitochondrial localization patterns depend on specific dendrite branch scaling rules.

Donovan et al., 2024, Cell Reports *43*, 114190
May 28, 2024
https://doi.org/10.1016/j.celrep.2024.114190

CellPress

Cell Reports

CellPress
OPEN ACCESS

Article

Dendrite architecture determines mitochondrial distribution patterns *in vivo*

Eavan J. Donovan,[1,3] Anamika Agrawal,[2,3] Nicole Liberman,[1] Jordan I. Kalai,[1] Avi J. Adler,[1] Adam M. Lamper,[1] Hailey Q. Wang,[1] Nicholas J. Chua,[1] Elena F. Koslover,[2] and Erin L. Barnhart[1,4,*]

[1]Department of Biological Sciences, Columbia University, New York, NY 10027, USA
[2]Department of Physics, University of California, San Diego, La Jolla, CA 92092, USA
[3]These authors contributed equally
[4]Lead contact
*Correspondence: eb3305@columbia.edu
https://doi.org/10.1016/j.celrep.2024.114190

SUMMARY

Neuronal morphology influences synaptic connectivity and neuronal signal processing. However, it remains unclear how neuronal shape affects steady-state distributions of organelles like mitochondria. In this work, we investigated the link between mitochondrial transport and dendrite branching patterns by combining mathematical modeling with *in vivo* measurements of dendrite architecture, mitochondrial motility, and mitochondrial localization patterns in *Drosophila* HS (horizontal system) neurons. In our model, different forms of morphological and transport scaling rules—which set the relative thicknesses of parent and daughter branches at each junction in the dendritic arbor and link mitochondrial motility to branch thickness—predict dramatically different global mitochondrial localization patterns. We show that HS dendrites obey the specific subset of scaling rules that, in our model, lead to realistic mitochondrial distributions. Moreover, we demonstrate that neuronal activity does not affect mitochondrial transport or localization, indicating that steady-state mitochondrial distributions are hard-wired by the architecture of the neuron.

INTRODUCTION

For more than a century, neuroscientists have attempted to define a conserved set of design principles that govern neuronal morphology across cell types and animal species.[1] To delineate these principles, the field has focused primarily on how the shape of a neuron affects its ability to receive, process, and transmit signals within a neural circuit while also minimizing total wiring.[2–11] However, neurons are not just signal processing units. Neurons are also post-mitotic cells in which subcellular constituent elements (e.g., organelles) degrade over timescales substantially shorter than the lifetime of the cell and are therefore continually regenerated and distributed throughout the neuron.[12–14] From this perspective, neuronal processes are not only cables for conducting electrical signals; axonal and dendritic branches are also supply lines, or conduits for microtubule-based trafficking of young, healthy organelles. Recent work suggests that intracellular trafficking requirements may constrain dendritic branching patterns,[15,16] but there is no comprehensive theory or experimental evidence that relates neuronal architecture to intracellular transport and the maintenance of steady state, global distribution patterns of organelles.

In this work, we combined theory and experimental measurements to investigate how dendritic branching patterns affect the transport and global distribution of mitochondria, organelles essential for the maintenance of neuronal form and function. There is abundant evidence that mitochondria move in neurons, both in cell culture[17–20] and *in vivo*,[21–24] and the mechanics governing the motility of an individual mitochondrion are relatively clear.[14,25] In brief, the motor proteins kinesin and dynein transport mitochondria along microtubules.[26] Adaptor proteins link mitochondria to motor proteins, and anchoring proteins oppose mitochondrial movement.[27–29] Whether a particular mitochondrion moves, and in which direction, depends on the number and orientation of microtubule tracks, as well as the relative amount of force generated by populations of motor proteins versus anchoring interactions.[25] It remains unclear, however, how neurons regulate these molecular-scale interactions in order to maintain large-scale mitochondrial distribution patterns.

Neuronal activity could regulate the spatial distribution of mitochondria.[19,30,31] Neuronal activation drives local calcium signals at synapses, and high calcium levels arrest mitochondrial motility in cultured neurons.[19,30] Calcium-dependent arrest of mitochondrial movement could, in principle, enrich mitochondria in subcellular regions with high synaptic densities and high energetic demands. However, several studies have shown that calcium signals have no effect on mitochondrial movement in neurons *in vivo*.[23,32,33] Moreover, global mitochondrial localization patterns likely depend not only on local mitochondrial arrest rates, but also on the relative flux of mitochondria into different subcellular compartments; calcium transients (or other local signals) cannot trap mitochondria near active synapses if there are no motile mitochondria to trap. Microtubule numbers are proportional to the thickness of neuronal processes,[34,35] and we

therefore propose that neuronal branching patterns—specifically, the relative sizes of sister subtrees that sprout from each branchpoint, as well as the relative thicknesses of parent and daughter branches—determine mitochondrial flux rates and thus global localization patterns.

In this paper, we interrogated the relationship between neuronal architecture and mitochondrial distribution patterns in *Drosophila* HS (horizontal system) cells. There are three HS neurons per optic lobe (six per fly), and all HS neurons have highly branched dendritic arbors that localize to the first layer of the lobula plate, the third neuropil of the *Drosophila* visual system (Figures 1A and 1B). HS neurons are among the most extensively studied neurons in flies[36–42] and there is a clear link between HS dendrite morphology and the specific function of HS neurons: large HS dendrites pool synaptic inputs from a retinotopic array of more than one thousand neurons that selectively respond to specific local motion cues, allowing HS neurons to act as matched filters for large-scale optic flow patterns.[42,43] In addition, theoretical work suggests that HS dendrite branching patterns are optimized to form the proper synaptic connections while also minimizing total dendritic length.[44–46] Here, we combined *in vivo* measurements of mitochondrial localization and transport with mathematical modeling to demonstrate that steady-state mitochondrial distribution patterns also depend on the precise structural scaling of HS dendrites. Based on our results, we argue that a comprehensive set of design principles for dendrite morphology must include rules for the reliable intracellular transport and localization of organelles, in addition to the previously considered principles for proper signal processing and wiring economy.

RESULTS

Mitochondria are enriched in distal HS dendrites and equitably distributed across sister subtrees

To investigate the relationship between dendrite morphology and steady-state mitochondrial localization patterns, we first measured mitochondrial localization in HS dendrites. We used the GAL4/UAS binary expression system to selectively label HS neurons (with a red fluorescent cytoplasmic volume marker, tdTomato) and the mitochondria within them (with GFP localized to the mitochondrial matrix, mitoGFP) before imaging fixed *Drosophila* brains by confocal microscopy (Figures 1B–1D). We found that mitochondria are distributed throughout HS neurons and exhibit a range of morphologies: a branched reticulum in the cell body, elongated mitochondria with variable widths in the dendrites, and smaller, round mitochondria in the axon terminals (Figure S1A). We measured the fraction of the dendrite volume occupied by mitochondria (the mitochondrial volume density), and we found that although the absolute mitochondrial volume fraction varied across samples, it was consistently higher in distal dendrites compared with the primary dendrite (Figure 1E).

The high density of mitochondria in HS dendrites made it difficult to resolve individual mitochondria using conventional confocal microscopy. We therefore took advantage of publicly available ssTEM images of an entire fly brain (the "female adult fly brain" or FAFB)[47] to measure mitochondrial distribution patterns in HS neurons. We used existing HS skeletons, which were previously traced through the three-dimensional FAFB image volume,[48] to identify mitochondria within the six HS neurons in the FAFB dataset (Figure 1F). Then, we measured mitochondrial morphology as a function of subcellular compartment by reconstructing whole mitochondria within small portions of the axon or dendrite (Figures S1B and S1C). We found that the median volume of an individual mitochondrion was $\sim$0.5 μm^3 in both HS dendrites and axons (Figure S1D). We also found that dendrites, but not axons, often contained large, branched mitochondria that spanned multiple dendritic branches (Figures S1C and S1D), consistent with previously published measurements of mitochondrial morphology in vertebrate neurons.[49,50]

Next, to measure mitochondrial distribution patterns throughout the whole cell, we resampled each HS skeleton such that skeleton nodes were placed at regular 5 μm intervals along the skeleton. Then we extracted two-dimensional image slices centered around each node and reconstructed the HS neuronal segment and all mitochondria within it in each image (Figure 1G). We calculated total mitochondrial densities for each HS neuron and found that, on average, the total mitochondrial density in HS neurons is $\sim$20% (mitochondrial density = 0.19 $\pm$ 0.04 SE). We measured substantial variation in the total mitochondrial density across the six HS neurons in the FAFB dataset (Figure S1E), consistent with our measurement of total mitochondrial density based on confocal images (Figure 1E). Despite this variation in total mitochondrial density, we found that mitochondrial localization patterns were conserved across all six HS cells. First, we measured mitochondrial densities as a function of subcellular compartment and found consistently higher mitochondrial densities in the dendrites than in the axons (Figures 1H and S1F). Second, in dendrites but not axons, mitochondrial densities increased with distance from the soma, with densities approximately two times higher in the distal dendrites compared with the primary dendrite (Figures 1H–1J and S1G–S1H). Third, we measured mitochondrial densities across sister subtrees. At each branchpoint within a dendritic arbor, a parent branch splits into two daughter branches, and the entire arbor can be decomposed into successive pairs of sister subtrees (Figure 1K). We found that sister subtrees are often asymmetric, and that larger subtrees contain proportionally more mitochondria than their smaller sisters, resulting in equivalent mitochondrial densities across sister subtree pairs (Figure 1L). Altogether, these results show that mitochondria in HS dendrites follow a specific distribution pattern: equitable distribution across sister subtrees and enrichment in distal dendrites.

Anterograde and retrograde transport of mitochondria is balanced in primary HS dendrites

In cultured neurons, a substantial fraction of mitochondria are motile, but there is some debate about the amount of mitochondrial movement in neurons *in vivo*, particularly in adult animals.[14,32,51] To measure mitochondrial motility in HS neurons *in vivo*, we used confocal microscopy to acquire time-lapse images of primary HS dendrites, labeled with mitoGFP and tdTomato, in head-fixed *Drosophila* (Figures 2A–2D; Video S1). Mitochondria moved in both the anterograde (into the dendritic arbor) and retrograde (out of the dendritic arbor) directions (Figures 2C

CellPress
OPEN ACCESS

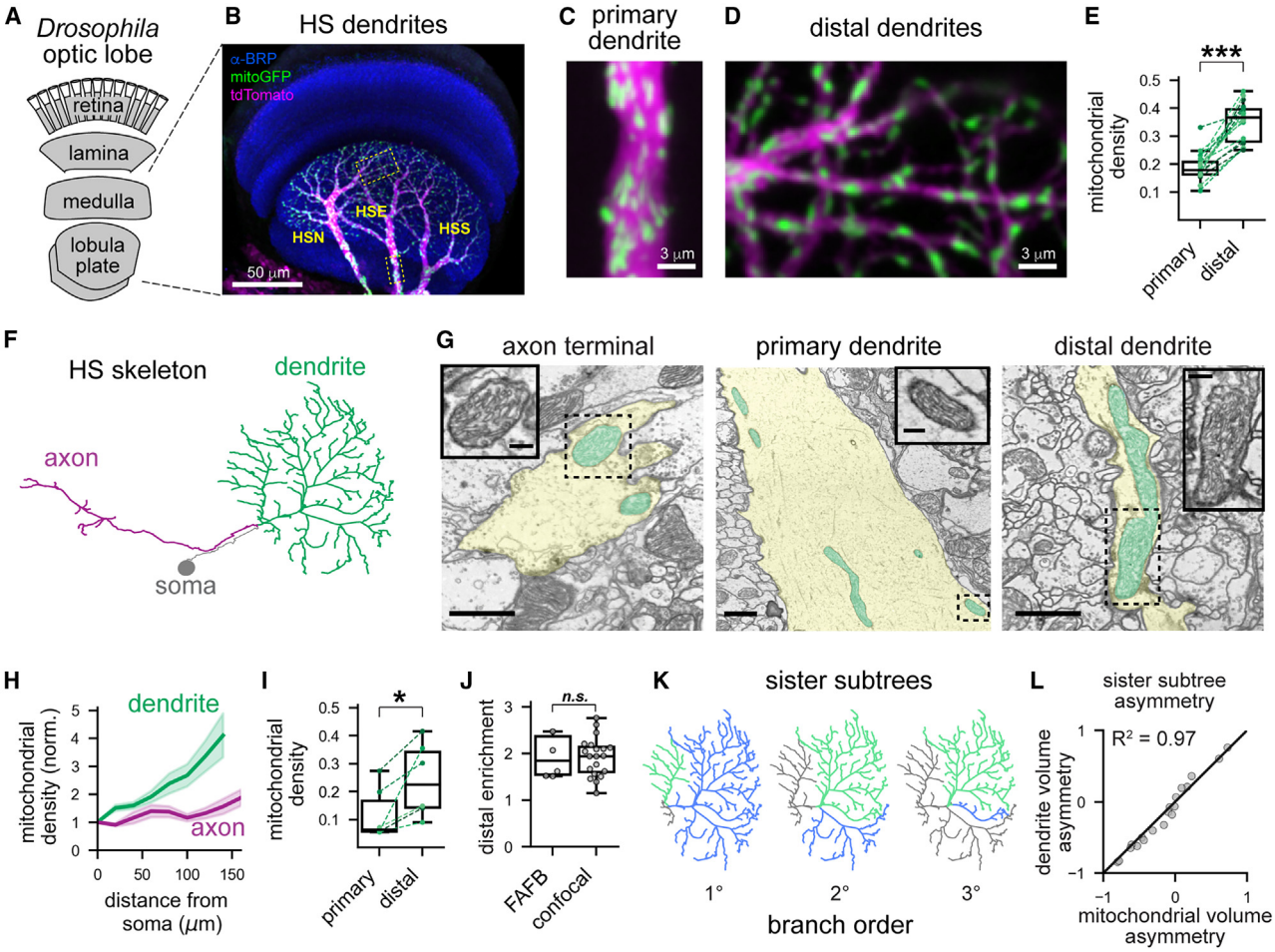

Figure 1. Mitochondria are enriched in distal HS dendrites and equitably distributed across sister subtrees

(A) Organization of the *Drosophila* visual system.

(B–D) Representative images of HS dendrites, and the mitochondria within them, labeled with a cytosolic volume marker (tdTomato, magenta) and a mitochondria-targeted GFP (mitoGFP, green). There are three HS neurons per optic lobe: HSN, HSE, and HSS. HS dendrites localize to the lobula plate, the third neuropil of the *Drosophila* optic lobe; neuropils were marked by immunostaining for the synaptic marker BRP (α-BRP, blue). Dashed yellow boxes in (B) indicate the primary and distal dendrites shown in (C) and (D). All images are maximum projections of confocal z stacks.

(E) Mitochondrial volume densities (the fraction of the cell volume occupied by mitochondria) in primary and distal HS dendrites, measured from confocal images. For all box and whisker plots (here and for all subsequent figures), the box extends from the first to third quartile of the data, with a line at the median, and the whiskers indicate 1.5 times the interquartile range. Dots overlaid on the boxplots indicate measurements from individual cells (N = 20 neurons); dotted lines connect measurements in the primary and distal dendrites of the same cell. The asterisks indicate a significant difference ($p < 0.001$, paired t test).

(F) Skeleton of an HS neuron traced through ssTEM images of an entire fly brain.[47,48]

(G) ssTEM images of mitochondria (cyan) in different compartments of an HS neuron (yellow). Scale bars, 1 μm. Dashed boxes indicate the regions enlarged in the inset images. Scale bars, 200 nm (inset).

(H) Average normalized mitochondrial densities, measured from ssTEM images, plotted versus distance from the soma in the dendrite (green) and axon (magenta). N = 6 neurons; shaded regions indicate the standard error of the mean. Mitochondrial densities were normalized to the density in the primary dendrite for each cell.

(I) Absolute mitochondrial volume densities in primary and distal HS dendrites, measured from ssTEM images. The asterisk indicates a significant difference ($p < 0.05$, paired t test).

(J) Distal enrichment of mitochondria, measured from both ssTEM and confocal images.

(K) HS dendrite skeletons showing pairs of sister subtrees at primary (1°), secondary (2°), and tertiary (3°) branchpoints.

(L) Asymmetry in total mitochondrial volume plotted versus asymmetry in total neurite volume for sister subtree pairs (N = 12 subtree pairs). Asymmetry = $(ST_1 - ST_2)/(ST_1 + ST_2)$, where ST_1 and ST_2 are metrics (dendrite volume or mitochondrial volume) on the two sister subtrees. See also Figure S1.

and 2D). Motile mitochondria ranged in length from ~0.5 to 5 μm, comparable with the majority of the mitochondria we observed in ssTEM images (Figures 1G, S1C, and S1D), and there was no significant difference in the average lengths of anterograde versus retrograde mitochondria (Figure 2E). Within the entire population of motile mitochondria (pooled across 19 primary dendrites from 19 flies), anterograde mitochondria exhibited higher speeds (0.66 ± 0.02 μm/s, N = 243 mitochondria) than

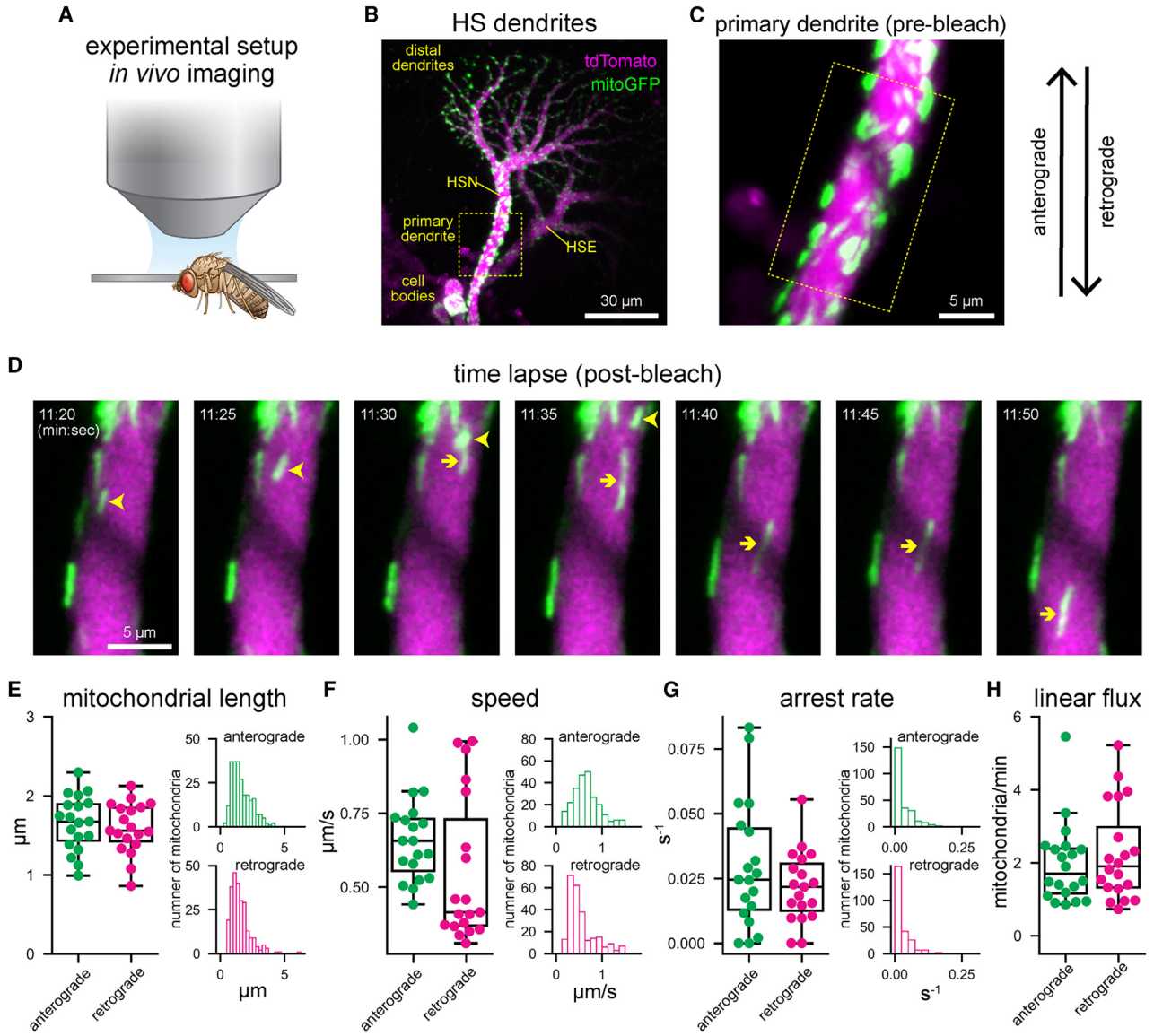

Figure 2. Anterograde and retrograde mitochondrial transport rates are balanced in primary HS dendrites

(A) Experimental setup: *in vivo* confocal imaging of head-fixed *Drosophila*.

(B and C) *In vivo* confocal images of mitochondria (mitoGFP, green) in HS dendrites (marked by cytosolic tdTomato, magenta) before (B) and after (C) photobleaching of stationary mitochondria in the primary dendrite. The dashed yellow box in (B) indicates the primary dendrite shown in (C).

(D) Image time series showing mitochondrial transport in the primary dendrite shown in (B) and (C). Stationary mitochondria were photobleached prior to image acquisition to facilitate resolution of motile mitochondria. The yellow arrowhead indicates a mitochondrion moving the anterograde direction; the yellow arrow indicates a mitochondrion moving in the retrograde direction.

(E–H) Lengths (E), speeds (F), arrest rates (G), and linear flux rates (H) for mitochondria moving in the anterograde (green) or retrograde (magenta) directions. Dots overlaid on the boxplots indicate average measurements for individual flies (N = 19 flies); there were no significant differences between average anterograde and retrograde measurements ($p > 0.05$, paired t test). Histograms show the distribution of measurements for individual mitochondria moving in the anterograde (N = 243 mitochondria) or retrograde (N = 250 mitochondria) directions; there is a significant difference in speed for the population of anterograde versus retrograde mitochondria ($p < 0.001$, unpaired t test). See also Figure S2.

retrograde mitochondria (0.55 ± 0.02 µm/s [SE], N = 250 mitochondria, $p < 0.001$, unpaired t test). However, there was no consistent difference in the average speed of anterograde versus retrograde mitochondria moving through the same primary dendrite (Figure 2F, $p = 0.09$, paired t test), and anterograde and retrograde mitochondria arrested motility at comparable rates (Figure 2G). Most motile mitochondria moved rapidly through the field of view and, on average, we were only able to track individual mitochondria for ~45 s. Despite this, the total distance traveled per mitochondrion was ~17 µm (average total distance = 17.2 ± 0.4 and 17.4 ± 0.4 µm [SE] for anterograde and retrograde mitochondria, respectively), suggesting that motile

mitochondria can travel throughout the dendrite rather than simply relocating by a few microns. Finally, we quantified the linear flux rate—the number of mitochondria moving through the primary dendrite per minute—and found no significant difference for anterograde versus retrograde transport (Figure 2H, average linear flux = 2.0 ± 0.2 and 2.3 ± 0.3 mitochondria/min for anterograde and retrograde transport, respectively; $p = 0.18$, paired t test). Altogether, these results demonstrate that, in HS cells, anterograde transport of mitochondria into the dendrite is balanced by retrograde transport of an equivalent volume of mitochondria back out of the dendrite.

Based on our measurements of linear flux rates and the typical size of motile mitochondria, we estimate (see STAR Methods) that approximately one cubic micron of mitochondrial volume exchanges through the primary dendrite every minute. By comparing this exchange rate ($J = 1\ \mu m^3$) to the volume density of mitochondria in the primary dendrite, we calculate that only a small fraction of mitochondria (~2%) are motile at any given instant. However, over longer timescales the total mitochondrial volume that exchanges through the primary dendrite (~60 μm^3/h) is a sizable fraction of the total mitochondrial volume in the entire dendrite arbor (~15%). These estimates indicate that, even if only a small number of mitochondria are motile at any given time, the entire mitochondrial population can reorganize over longer times scales (hours to days). In HS dendrites, we estimate that the entire mitochondrial volume reorganizes in less than 10 h, or more than 100 times over the course of a fly's lifetime. Altogether, our *in vivo* motility measurements indicate that the specific mitochondrial localization pattern in HS dendrites reflects a dynamic steady state in which individual mitochondria continually reorganize within a stable global pattern.

Mitophagy is largely restricted to the cell body in HS neurons

In addition to moving throughout the cell, mitochondria are degraded and replaced in neurons.[14] In principle, the spatial pattern of mitochondrial degradation—which occurs, in part, by mitochondrial autophagy, or mitophagy—could shape the global distribution of mitochondria in HS dendrites. To measure the spatial pattern of mitophagy in HS neurons, we used the mitophagy reporter mitoQC,[52] which consists of tandem fluorescent proteins (GFP and mCherry) targeted to the mitochondrial outer membrane (Figure S2). When mitoQC-tagged mitochondria undergo mitophagy, the acidic environment of the lysosome quenches GFP, allowing visualization of mitolysosomes as red-only puncta. We used *in vivo* confocal microscopy to image mitoQC in HS neurons and calculated a mitophagy index—the volume of mitolysosomes (red-only) divided by the volume of mitochondria (red + green)—for HS primary and distal dendrites and cell bodies. We observed almost no mitolysosomes in HS dendrites (Figures S2B–S2D). In the cell body, we measured an average mitophagy index of 0.07 (SE = 0.01), indicating that ~7% of the mitochondrial volume in the cell body was undergoing degradation in lysosomes (Figures S2A and S2D). Thus, even if mitochondria are autophagocytosed in the dendritic branches, they remain undegraded until reaching the cell body, similar to recent observations of autophagic vesicles in cultured neurons.[53] Altogether, these measurements suggest that mitochondrial degradation plays a negligible role in shaping the mitochondrial localization pattern in the dendrite.

A mathematical model for mitochondrial transport in branched dendrites links mitochondrial localization patterns to dendrite architecture

How do HS dendrites maintain stable mitochondrial localization patterns despite constant transport and reorganization of mitochondrial mass? We hypothesized that dendrite architecture determines steady-state mitochondrial localization patterns in HS neurons. To test this idea, we developed a mathematical model linking mitochondrial transport and localization patterns to dendrite morphology (Figures 3A–3C; see detailed model description in methods and model parameters and variables in Tables S1 and S2). In our model, each dendrite is a binary tree, where each node connects a parent edge to two daughter edges, and each edge is a cylinder with fixed radius r_i along its entire length l_i (Figure 3B). We set the topology of the dendritic arbor—the length and connectivity of each branch—based on dendritic skeletons extracted from real HS neurons (Figure 3A) or from synthetic trees (Figure S3A), and we impose branch radii according to two morphological scaling rules. The first scaling rule dictates the relative widths of the parent and daughter branches (parent-daughter scaling). Consistent with several previous studies,[2,54–56] we assume that parent and daughter radii scale according to the power law $r_0^\alpha = r_1^\alpha + r_2^\alpha$, where r_0 is the radius of the parent branch, r_1 and r_2 are the radii of the daughter branches, and the exponent α determines whether total dendritic cross-sectional area in the daughter branches, relative to the parent branch, increases ($\alpha > 2$), decreases ($\alpha < 2$), or remains the same ($\alpha = 2$). The second scaling rule—$r_1/r_2 = \mu$—sets the relative widths of the two daughter branches (sister-sister scaling); in the simplest version of sister-sister scaling, the widths of the two daughter branches are equal ($\mu = 1$).

Within the dendrite, we assume that mitochondria can be motile or stationary (Figure 3C). Motile mitochondria move in a processive fashion in the anterograde or retrograde direction with pause-free velocity $v_i^\pm$ and arrest motility at rate $k_{s,i}$. Stationary mitochondria initiate motility at rate $k_{w,i}$. In the first, simplest version of our model, we assume that mitochondrial velocities and stopping and starting rates are constant throughout the dendritic arbor. In subsequent versions of the model, we allow arrest rates to scale with dendrite radius according to $k_{s,i} \sim 1/r_i^\beta$, where the exponent β determines whether arrest rates increase ($\beta > 0$), decrease ($\beta < 0$), or remain the same ($\beta = 0$) as dendrite radii decrease. At steady state, the linear densities of anterograde, retrograde, and stationary mitochondria in each dendritic branch (ρ_i^+, ρ_i^-, and ρ_i^s, respectively), obey the transport equations:

$$\frac{d\rho_i^\pm}{dt} = \mp v_i \frac{d\rho_i^\pm}{dx} - k_{s,i}\rho_i^\pm + \frac{k_{w,i}}{2}\rho_i^s = 0$$
$$\frac{d\rho_i^s}{dt} = k_{s,i}\left(\rho_i^+ + \rho_i^-\right) - k_{w,i}\rho_i^s = 0 \quad \text{(Equation 1)}$$

The steady-state solutions of these transport equations are constant linear mitochondrial densities within each individual branch, and the relative linear densities between branches are

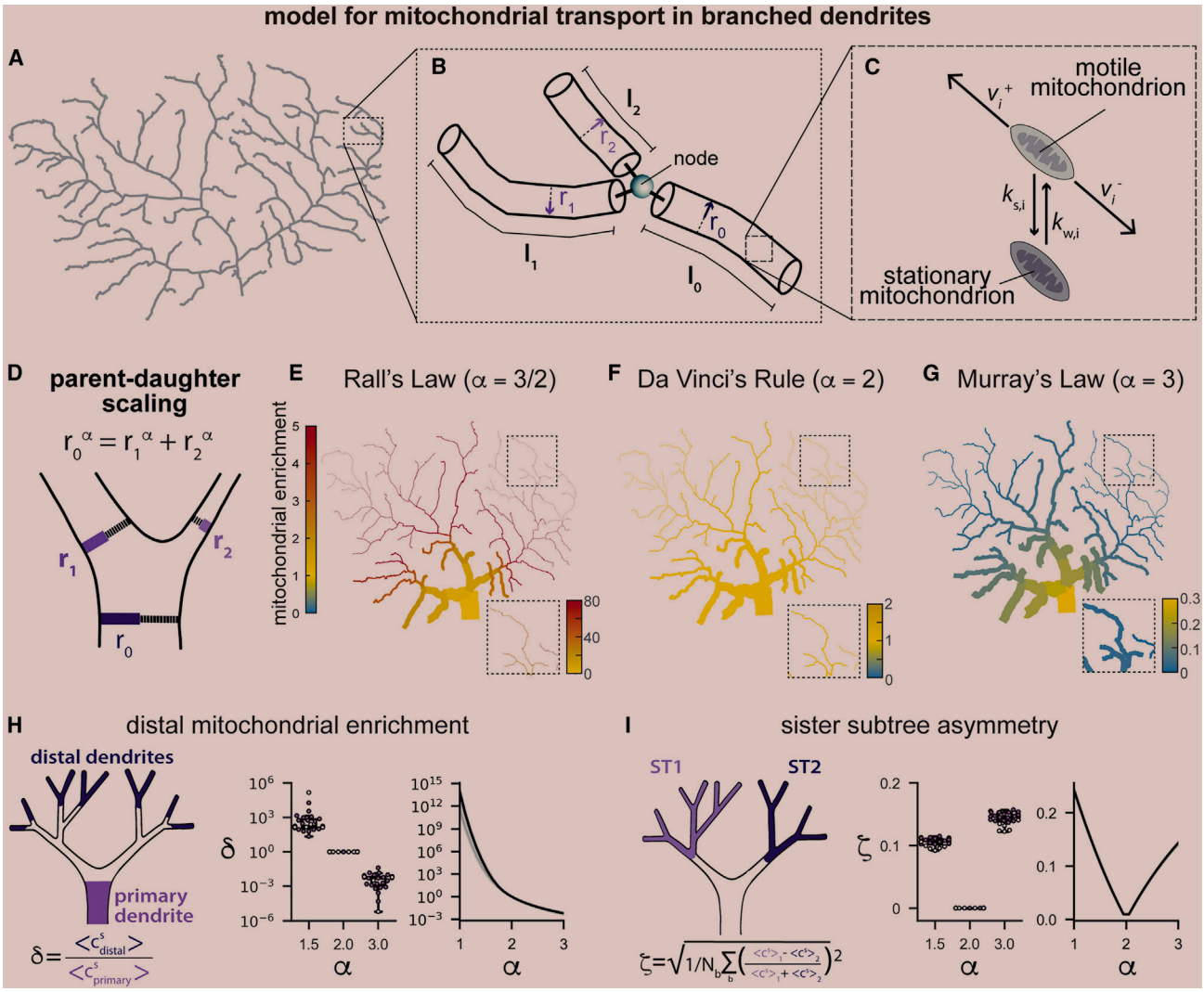

Figure 3. A mathematical model for mitochondrial transport in branched dendrites

(A–C) Schematic representation of a mathematical model linking mitochondrial transport and localization to dendrite morphology. Mitochondria move through a branched dendritic tree (A), with dendrite topology extracted from an HS skeleton traced through ssTEM images.[47,48] At each branchpoint, a parent branch splits into two daughter branches (B). Each branch is a cylinder with fixed radius r_i along its entire length l_i, where l_i is set by dendrite skeletons extracted from real HS neurons (A) and r_i is set by morphological scaling rules dictating the relative thicknesses of the parent radius and the two daughter radii (parent-daughter scaling and sister-sister scaling, see main text). Within each branch (C), motile mitochondria move in a processive fashion in the anterograde or retrograde direction at velocity v_i. Motile mitochondria arrest motility at rate $k_{s,i}$ and stationary mitochondria initiate motility at rate $k_{w,i}$.

(D) Parent-daughter scaling: parent and daughter radii scale according to $r_0^{\alpha} = r_1^{\alpha} + r_2^{\alpha}$, where r_0 is the radius of the parent branch, r_1 and r_2 are the radii of the daughter branches, and the exponent α determines whether the total cross-sectional area constricts, expands, or remains the same across the branchpoint.

(E–G) Model predictions of mitochondrial localization patterns for parent-daughter scaling according to Rall's law ($\alpha = 3/2$, E), Da Vinci's rule for trees ($\alpha = 2$, F), and Murray's law ($\alpha = 3$, G). Radii were imposed according to the indicated values for the parent-daughter scaling exponent α; each branch is colored according to mitochondrial density compared with the primary dendrite (yellow indicates the same density as in the primary dendrite; red and blue indicate mitochondrial enrichment and dilution, respectively).

(H and I) Model predictions for mitochondrial distal enrichment (H) and distribution across sister subtrees (I) for topologies extracted from skeletons traced through ssTEM images[47] (open circles, $N = 6$ dendrites) and previously published reconstructions[46] (purple circles, $N = 20$ dendrites). Boxplots show distal enrichment or asymmetry in mitochondrial densities across sister subtrees for model dendrites obeying Rall's law, Da Vinci's rule for trees, or Murray's law for parent-daughter scaling; dots overlaid on the boxplots indicate model predictions for individual dendrite topologies. Line plots show distal enrichment or sister subtree asymmetry for a range of values for the parent-daughter scaling parameter α ($1 \leq \alpha \leq 3$); the shaded region indicates the standard error of the mean. Distal enrichment (δ) and sister subtree asymmetry (ζ) were calculated according to the indicated metrics (see STAR Methods for details). See also Figure S3 and Tables S1 and S2.

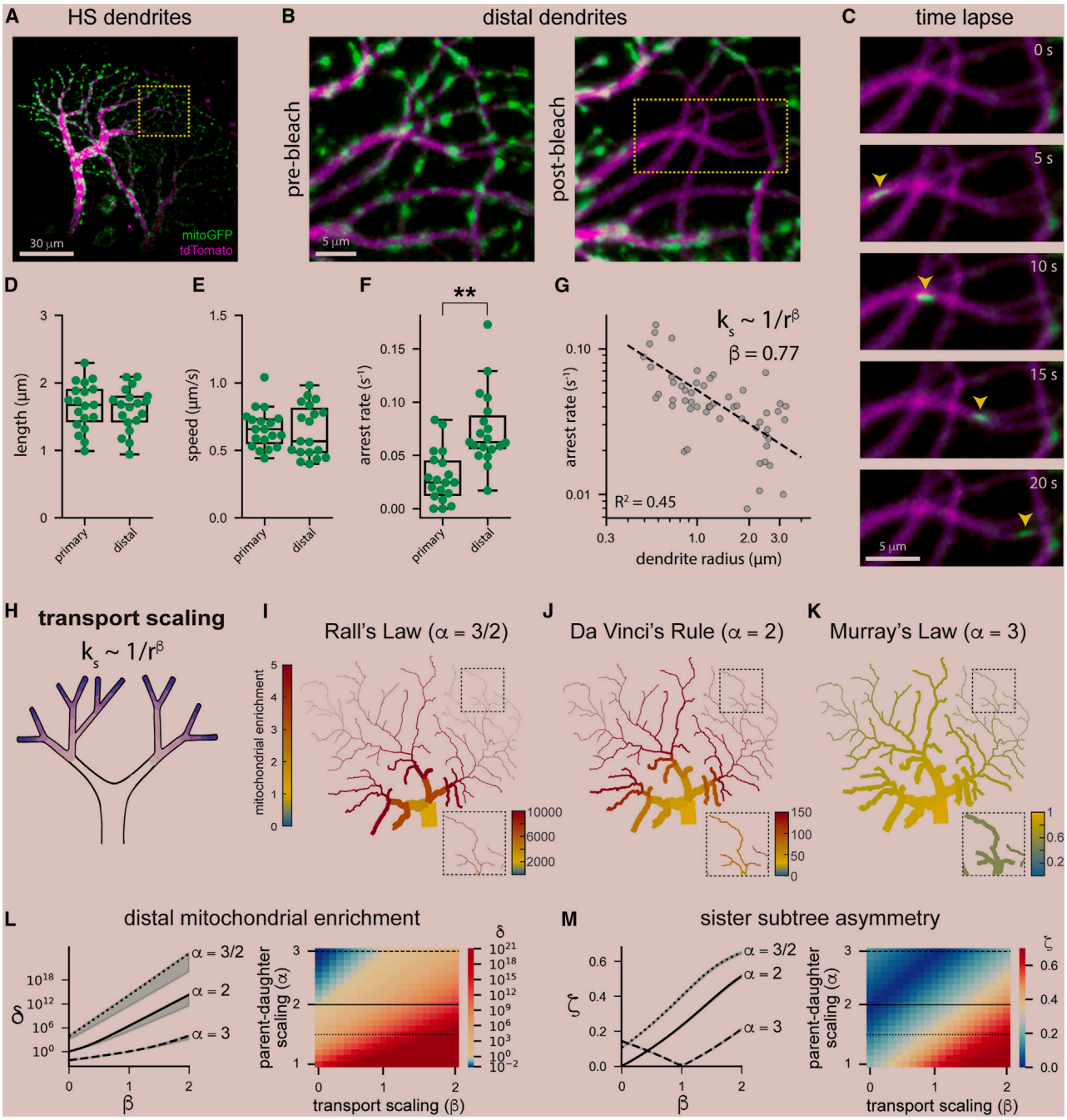

Figure 4. Mitochondrial arrest rates scale with dendrite radius

(A and B) *In vivo* confocal images of mitochondria (mitoGFP, green) in HS dendrites (marked by cytosolic tdTomato, magenta) before photobleaching of stationary mitochondria in the distal dendrites. The dashed yellow box in (A) indicates the distal dendrites show in (B).

(C) Image time series showing a mitochondrion (indicated by yellow arrowheads) moving in the anterograde direction through a distal dendritic branch.

(D–F) Boxplots showing mitochondrial lengths (D), speeds (E), and arrest rates (F) for mitochondria moving in the anterograde direction through primary and distal dendrites; primary dendrite measurements from Figure 1 are shown again here for ease of comparison. Dots overlaid on boxplots show average measurements for individual flies (D–F, N = 19 flies). Asterisks indicate significant differences ($p < 0.01$, paired t test).

(G) The average mitochondrial arrest rate in dendritic branches plotted versus dendrite radius (N = 47 branches from 41 flies). Arrest scales with dendrite radius according to $k_s \sim 1/r^\beta$, where $\beta = 0.77$ (dashed line, $R^2 = 0.45$).

(H) Cartoon depicting mitochondrial transport scaling according to $k_s \sim 1/r^\beta$.

(I–K) Model predictions of mitochondrial localization patterns based on the experimentally measured value of the transport scaling parameter $\beta = 0.8$, with constants $\psi = 1$ and $\mu = 1$, and parent-daughter scaling according to Rall's law ($\alpha = 3/2$, I), Da Vinci's rule for trees ($\alpha = 2$, J), and Murray's law ($\alpha = 3$, K).

(legend continued on next page)

determined by the boundary conditions at branch junctions. At distal dendrite tips, we assume reflecting boundary conditions ($\rho^+ = \rho^-$), and we set the boundary condition in the trunk of the dendritic by fixing the linear density of motile mitochondria to a constant ρ^*. At branchpoints, we assume that linear mitochondrial flux rates are conserved across parent and daughter branches: $v_0\rho_0^{\pm} = v_1\rho_1^{\pm} + v_2\rho_2^{\pm}$. Finally, we set the relative linear flux of anterograde mitochondria in the two daughters at each junction according to the scaling rule $\frac{v_1\rho_1^+}{v_2\rho_2^+} = \psi$; in the simplest version of this junction-flux scaling rule, linear fluxes in the two daughters are equal ($\psi = 1$).

We implemented several versions of this model using different forms of morphological and transport scaling rules (see STAR Methods). We found steady-state linear mitochondrial densities through analytical solutions of the set of linear equations described above, and we computed the mitochondrial volume density in each branch as $c_i = \frac{\rho_i}{r_i^2}$. For all model versions, we quantified mitochondrial localization patterns using two metrics—sister subtree asymmetry (ζ, the root-mean-squared asymmetry of stationary mitochondrial volume densities between sister subtrees, averaged over all junctions in the arbor) and distal enrichment (δ, the stationary mitochondrial volume density in distal dendrites normalized to the primary dendrite)—to compare model predictions to our experimental measurements.

We first examined the relationship between different forms of power law parent-daughter scaling (Figure 3D, $r_0^{\alpha} = r_1^{\alpha} + r_2^{\alpha}$) and mitochondrial localization patterns. Optimal values for the exponent α have been derived based on theoretical arguments for preservation of graded electrical signals across dendritic branchpoints ($\alpha = 3/2$, often called "Rall's law" after the neuroscientist Wilfrid Rall),[2] action potential propagation in axons ($\alpha = 3$, often called "Murray's law" and first derived for the vasculature system),[54,55,57] or efficient intracellular transport ($\alpha = 2$, often called "Da Vinci scaling" after Da Vinci's rule for trees).[56,58] To determine how α affects steady-state mitochondrial localization patterns, we calculated sister subtree asymmetry and distal enrichment of mitochondrial densities for a range of values for α. We assumed the simplest versions of sister-sister scaling and transport scaling—equal splitting of sister branch radii ($\mu = 1$), equal linear flux rates in sister branches ($\psi = 1$), and spatially uniform transport rates ($\beta = 0$)—and we set the topology of the arbor based on HS skeletons (Figures 3E–3I) or synthetic dendritic trees (Figures S3A–S3C). When parent and daughter radii obey Da Vinci's rule for trees ($\alpha = 2$), this simple model yields mitochondrial volume densities that are constant throughout the entire arbor, resulting in equitable distribution of mitochondria across sister subtrees but not distal enrichment (Figures 3F, 3H–3I, S3B, and S3C). In contrast, when parent and daughter dendrites scale according to Rall's law ($\alpha = 3/2$), mitochondria are enriched in distal dendrites (Figures 3E–3H and S3B), and when dendrites scale according to Murray's law ($\alpha = 3$), mitochondria are diluted distally (Figures 3G, 3H, and S3B). Overall, the relative density of mitochondria in the distal versus primary dendrites increases as the exponent α decreases (Figures 3H and S3B).

Equitable distribution of mitochondria across sister subtrees also depends on the exponent α (Figures 3I and S3C). In contrast to Da Vinci-scaled dendrites ($\alpha = 2$), when model dendrites obey either Rall's law ($\alpha = 3/2$) or Murray's law ($\alpha = 3$), equitable distribution across sister subtrees occurs only when branching patterns are perfectly symmetric (Figure S3C); when branching patterns are asymmetric, as in real HS dendrites, mitochondrial densities in sister subtrees are asymmetric (Figure 3I). In particular, subtrees with more branchpoints tend to accumulate higher (in Rall-scaled dendrites; Figure 3E) or lower (in Murray-scaled dendrites; Figure 3G) mitochondrial volume densities due to the reduction or expansion of dendritic cross-sectional area below each branchpoint. Altogether, this initial version of our model recapitulates either equitable distribution of mitochondria across sister subtrees (in Da Vinci-scaled dendrites) or distal enrichment (in Rall-scaled dendrites), but not both.

Mitochondrial arrest rates scale with dendrite radius

We next sought to update our model to fully recapitulate our experimental measurements of mitochondrial localization patterns—distal enrichment and equitable distribution of mitochondria across asymmetrically branched sister subtrees. We reasoned that non-uniform transport parameters—e.g., mitochondrial arrest rates that increase as dendrites narrow across branchpoint—ought to result in distal mitochondrial enrichment even in Da Vinci-scaled dendrites. We therefore measured mitochondrial motility in primary versus distal HS dendrites using *in vivo* imaging (Figures 4A–4C; Video S2), focusing in particular on mitochondria moving in the anterograde direction due to experimental constraints (see STAR Methods). We found that motile mitochondria in the distal and primary dendrites are approximately the same length (Figure 4D) and move at the same speeds (Figure 4E), but mitochondrial arrest rates are significantly higher in the distal dendrites (Figure 4F). We analyzed motile mitochondria moving through dendritic branches with a range of radii and found that the rate of mitochondrial arrest $k_{s,i}$ scales with dendrite radius r_i according to $k_{s,i} \sim 1/r_i^{\beta}$, where the best fit for β is ~0.8 (Figure 4G).

Next, we updated our model to include scaling of mitochondrial arrest with dendrite radius according to $k_{s,i} = \frac{1}{r_i^{\beta}}$ (Figure 4H). For simplicity, we assumed that mitochondrial speeds and motility initiation rates are spatially uniform; different assumptions, including scaling of speed or motility initiation rate $k_{w,i}$ with dendrite radius, do not affect model predictions when the fraction of motile mitochondria is small (see STAR Methods),

(L and M) Model predictions for mitochondrial distal enrichment (L) and distribution across sister subtrees (M) are shown for topologies extracted from skeletons traced through ssTEM images[47] (open circles, $N = 6$ dendrites) and previously published reconstructions[46] (light purple circles, $N = 20$ dendrites). Line plots show distal enrichment or asymmetry in mitochondrial densities across sister subtrees for model dendrites obeying Rall's law (dashed line), Da Vinci's rule for trees (solid line), or Murray's law (dotted line). Heatmaps show average distal enrichment or sister subtree asymmetry for a range of values for the transport scaling parameter β ($0 \leq \beta \leq 2$) and the parent-daughter scaling parameter α ($1 \leq \alpha \leq 3$).

as we observed experimentally. When we set β according to our experimental measurements ($\beta = 0.8$), our model predicts distal enrichment in Da Vinci-scaled dendrites as well as Rall-scaled dendrites (Figures 4I and 4J), but not in Murray-scaled dendrites (Figure 4K). Altogether, the amount of distal enrichment decreases with the parent-daughter scaling parameter α and increases with the transport scaling parameter β (Figures 4L and S3D).

Introducing inverse scaling of mitochondrial arrest with dendrite radius according to $k_{s,i} = \frac{1}{r_i^{\beta}}$ results in distal enrichment in model dendrites that follow Da Vinci's rule. However, this transport scaling also introduced significant asymmetries in mitochondrial densities across sister subtrees, even in Da Vinci-scaled dendrites (Figures 4M and S3E). In particular, subtrees with more branchpoints acquire higher mitochondrial densities, resulting in inequitable distribution across subtrees in arbors with asymmetric topologies (Figure 4J). In Rall-scaled dendrites, transport scaling resulted in even higher asymmetry across sister subtrees than in the initial version of our model (Figures 4M and S3E). Interestingly, in Murray-scaled dendrites, transport scaling with $\beta = 1$ resulted in constant mitochondrial volume densities throughout the arbor and therefore equitable distribution across sister subtrees (Figures 4M and S3E) but not distal enrichment (Figures 4L and S3D). Thus, some combinations of the parent-daughter scaling parameter α and the transport scaling parameter β recapitulate either distal enrichment (e.g., $\alpha = 2$ and $\beta > 0$) or equitable distribution across sister subtrees ($\alpha = 3$ and $\beta = 1$) but not both.

Mitochondria split according to dendrite thickness at asymmetric branchpoints

HS dendrites are asymmetrically branched, such that one sister subtree is often significantly larger than the other (Figures 1K and 5A). We reasoned that equitable distribution of mitochondria across asymmetrically sized subtrees could be achieved if proportionally more mitochondria move into the larger subtree at each branchpoint. Such proportional splitting of mitochondria at branchpoints would occur if linear flux rates scale with daughter branch thickness (junction-flux scaling according to $\psi = \frac{v_1\rho_1}{v_2\rho_2} = \frac{r_1^2}{r_2^2}$) and thicker trunks support proportionally larger subtrees. To explore this idea, we measured branch thickness and mitochondrial transport at primary branchpoints in HS dendrites. We found, first, that mitochondria move persistently across branchpoints in both the anterograde (Figure 5B) and retrograde directions, with very few motile mitochondria arresting (15% ± 1%) or reversing direction (0.4% ± 0.2%) at the junction. Average mitochondrial linear flux rates were significantly lower in the daughter branches than in the parent branch (Figure 5C), but there was no significant difference in flux normalized to branch cross-sectional area (Figures 5D and 5E). This conservation of flux, which we also measured in primary versus distal dendrites (Figure 5F), is consistent with spatially uniform volume densities of motile mitochondria, a hallmark of Da Vinci-scaled dendrites in our model (see STAR Methods). Finally, we found that asymmetric linear flux (indicating that more mitochondria move into one daughter than the other) correlates with asymmetric daughter branch cross-sectional areas (Figure 5G). Thus, proportionally more mitochondria move into thicker daughter branches at each branchpoint (Figure 5H). This proportional splitting of mitochondria between daughter branches is consistent with equivalent microtubule densities in each daughter, as previously observed in other neuronal cell types.[34,35]

Specific sister subtree scaling rules recapitulate realistic mitochondrial localization patterns in model dendrites

Based on our experimental measurements of mitochondrial transport across branchpoints, we updated our model to include scaling of linear flux with daughter branch thickness: $\psi = \frac{r_1^2}{r_2^2}$. This scaling rule for transport across branchpoints could facilitate equitable distribution of mitochondria across asymmetric sister subtrees if thicker trunks support proportionally larger subtrees at each branchpoint. Several parameters quantify subtree size (e.g., total length or volume), and trunk thickness could scale with any of these parameters. Importantly, we were able to derive the sister-sister scaling rule required for equitable distribution of mitochondria for a specific subset of parent-daughter and transport scaling parameters. Specifically, when parent and daughter radii obey Da Vinci's rule for trees ($\alpha = 2$), mitochondrial arrest scales with dendrite radius according to $k_{s,i} \sim 1/r_i^2$ ($\beta = 2$), and motile mitochondria split according to daughter thickness at branchpoints ($\psi = \frac{r_1^2}{r_2^2}$), our analytical calculations (see STAR Methods) show that equitable distribution of mitochondria depends on a specific morphological relationship between sister subtrees: the total subtree volume must be proportional to its length, such that $L_1/V_1 = L_2/V_2$. In addition, in a Da Vinci-scaled arbor, all subtrees will exhibit this length-volume scaling if and only if sister trunk thicknesses scale according to $\mu = \frac{r_1^2}{r_2^2} = \frac{L_1/D_1}{L_2/D_2}$, where D describes the effective depth of the tree (see STAR Methods). The ratio of total length over depth (L/D) can be thought of as the "bushiness" of a tree; $L/D = 1$ in a dendrite with no branches, whereas $L/D \gg 1$ in a highly branched, bushy dendrite.

Our derivation of this specific sister-sister scaling rule, where sister subtree trunk thickness is proportional to subtree bushiness ($r^2 \sim L/D$, Figure 6A), is based on a special case where mitochondrial arrest scales according to $k_{s,i} \sim 1/r_i^2$ ($\beta = 2$), but we measured $\beta = \sim 0.8$ from our experimental data (Figure 4G). Changes in β have a dramatic effect on distal enrichment of mitochondria, and $\beta = 0.8$ results in more realistic levels of enrichment than $\beta = 2$ (Figures 6B, 6C, and S3F). In contrast, equitable distribution of mitochondria across subtrees is robust to changes in β, but only in dendrites that obey both Da Vinci's parent-daughter scaling and $r^2 \sim L/D$ sister-sister scaling (Figures 6D and S3G). Da Vinci-scaled dendrites that follow different sister subtree scaling rules do not exhibit such equitable distributions across subtrees (Figures 6D and S4A), nor do Rall- or Murray-scaled dendrites that obey $r^2 \sim L/D$ (Figure 6D). Moreover, we show that, for an arbor obeying Rall's law, it is impossible to establish equitable mitochondrial distributions between asymmetric sister subtrees with any single function that sets sister subtree trunk thicknesses based on subtree

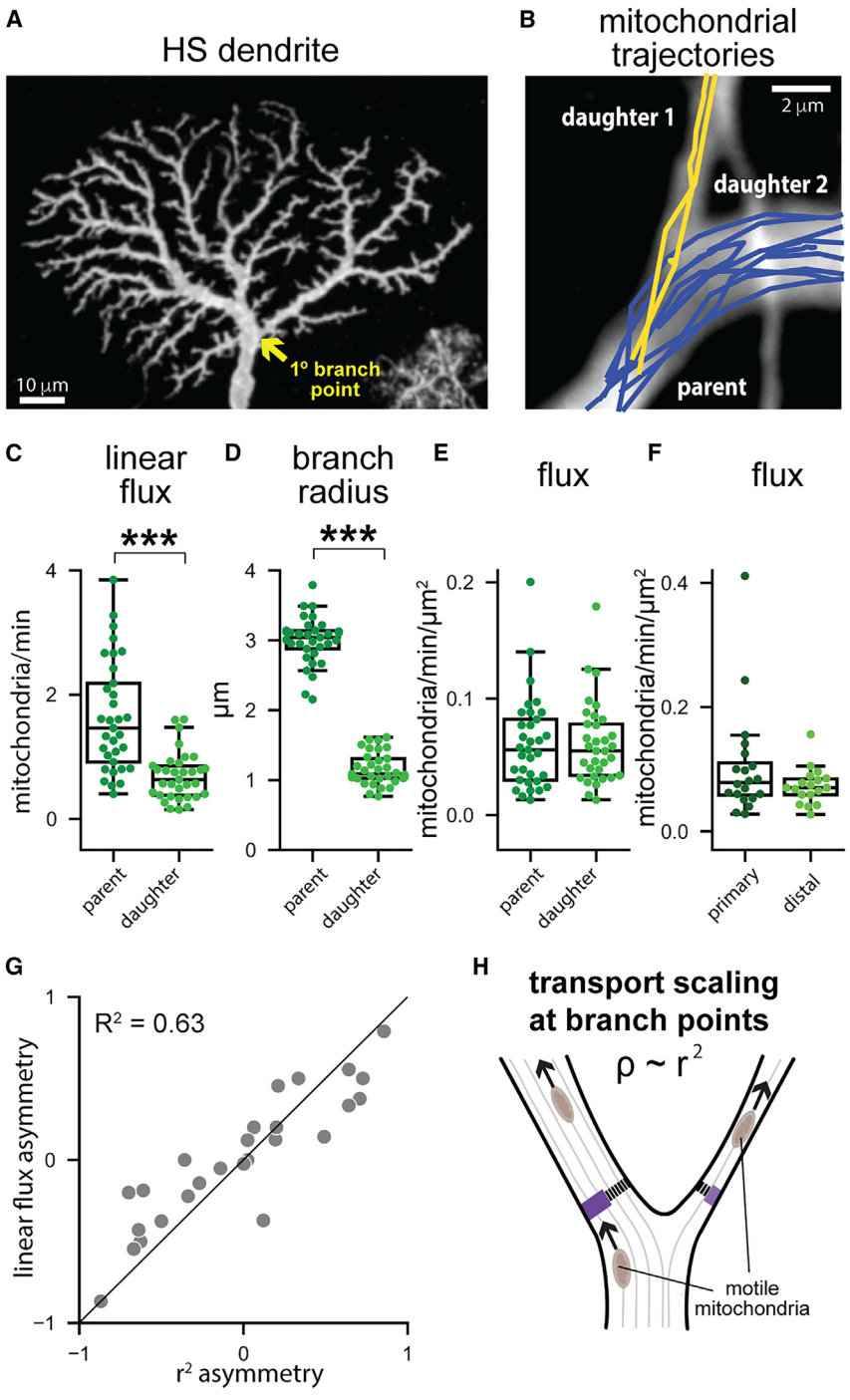

Figure 5. Motile mitochondria split according to dendrite thickness at asymmetric branchpoints

(A) HS dendrite, labeled by MultiColor FlpOut (MCFO). The yellow arrow indicates the primary branchpoint.

(B) Trajectories of mitochondria moving in the anterograde direction from a parent branch into one of two daughter branches. Trajectory colors indicate mitochondria that moved into daughter one (yellow) or daughter two (blue).

(C–F) Boxplots showing mitochondrial linear flux (C), dendrite radius (D), and linear flux normalized to dendrite cross-sectional area (E and F) for parent and daughter branches (C–E) and primary versus distal dendrites (F). Asterisks indicate significant differences ($p < 0.001$, paired t test).

(G) Asymmetry in daughter branch radii squared plotted versus asymmetry in mitochondrial linear flux rates. Dots indicate measurements from individual branchpoints ($N = 26$ branchpoints from 26 flies).

(H) Cartoon depicting equitable splitting of mitochondria across branchpoints, where the linear flux of anterograde mitochondria is proportional to daughter branch cross-sectional area: $\rho \sim r^2$.

HS dendrites obey specific morphological scaling rules

To determine whether HS dendrites scale parent and daughter branches according to Da Vinci's rule and sister branches according to $r^2 \sim L/D$, we used stochastic MultiColor FlpOut labeling[59] to label individual HS dendrites (Figure 6E). We segmented and skeletonized each dendrite before measuring parent and daughter branch radii and the length, volume, and bushiness of the subtrees sprouting from each branchpoint (Figures 6E and 6F). Consistent with our previous observations, we found that HS dendrites are asymmetrically branched, with significant asymmetry in daughter branch thickness and subtree length, volume, and bushiness (Figure 6G). We fit our measurements of parent and daughter radii to the power law $r_0^\alpha = r_1^\alpha + r_2^\alpha$ for a range of values for the exponent α, and we found that HS dendrites are approximately Da Vinci scaled, with $\alpha = 2.2$ giving the best fit (Figure 6H, $R^2 = 0.87$, 95% bootstrap confidence interval = 2–2.5).

Next, our model predicts that, when mitochondrial arrest rates scale with dendrite thickness, Da Vinci-scaled dendrites can only achieve equitable distribution of mitochondria if sister subtrees have volumes proportional to their length. To test this prediction, we compared the asymmetry in subtree lengths with the asymmetry in volumes for sister subtree pairs emerging from the morphology (Figure S5; see STAR Methods). Altogether, of all the parent-daughter and sister-sister scaling rules we examined, only one pair of rules—parent-daughter scaling according to Da Vinci's rule for trees and sister-sister scaling with trunk thickness proportional to subtree bushiness—successfully recapitulates the key features of experimentally observed mitochondrial distributions: equitable densities between sister subtrees and increased density in distal branches.

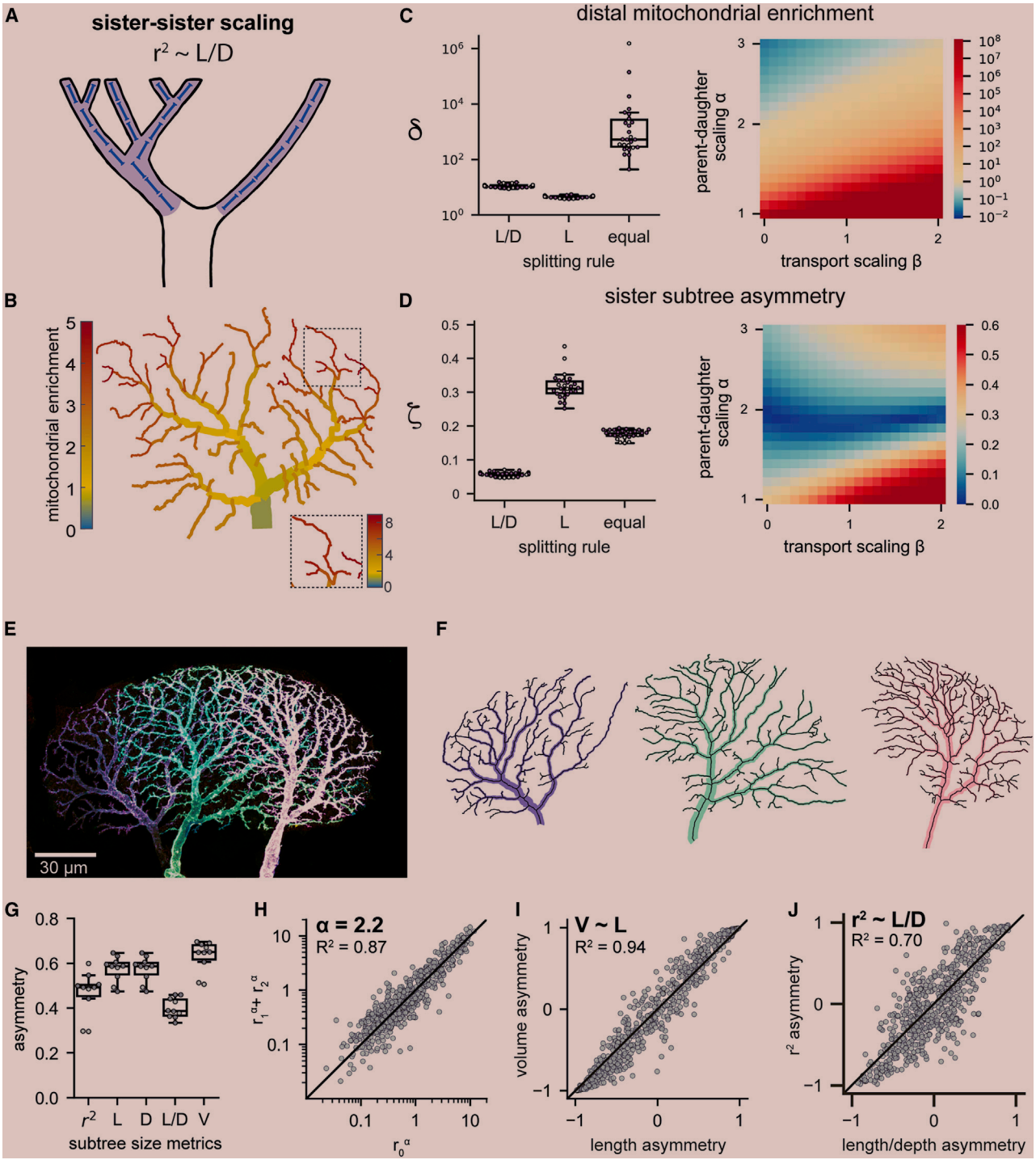

Figure 6. HS dendrites obey specific parent-daughter and sister-sister scaling rules

(A) Cartoon depicting sister-sister scaling where daughter branch cross-sectional area is proportional to subtree length/depth, or "bushiness": $r^2 \sim L/D$.

(B) Model predictions of mitochondrial localization patterns for specific morphological scaling rules (parent-daughter scaling according to Da Vinci's rule for trees ($\alpha = 2$) and sister-sister scaling according to $r^2 \sim L/D$) and transport scaling rules (inverse scaling of arrest with dendrite radius according to $k_s \sim 1/r^{\beta}$, where $\beta = 0.8$, and proportional splitting of mitochondria at branchpoints according to $\rho \sim r^2$).

(C and D) Boxplots show distal enrichment (C) or asymmetry in mitochondrial densities across sister subtrees (D) for model dendrites obeying the indicated forms of sister-sister scaling (radii splitting according to subtree bushiness [L/D], total subtree length [L], or equally [$r_1 = r_2$]), with $\beta = 0.8$; dots overlaid on the boxplots

(legend continued on next page)

same branchpoint. We found that length asymmetry is equal to volume asymmetry (Figure 6I, $R^2 = 0.94$), indicating that longer sister subtrees have proportionally larger volumes, as predicted. Thus, HS dendrites obey two separate morphological rules: power law scaling of parent and daughter branches with $\alpha \cong 2$, and sister subtree splitting with volume proportional to length ($L_1/V_1 = L_2/V_2$). According to our model, for dendrites that follow these two rules, daughter branch cross-sectional areas must be proportional to subtree bushiness ($r^2 \sim L/D$). To test this prediction, we compared asymmetry in branch cross-sectional area to asymmetry in subtree bushiness. We found that trunk cross-sectional area and bushiness asymmetry are well correlated (Figure 6J, $R^2 = 0.70$). In contrast, cross-sectional area asymmetry was only weakly correlated with subtree length, volume, or depth asymmetry (Figures S4B–S4D).

Altogether, these results indicate that HS dendrites obey the specific subset of morphological scaling rules that are predicted by our model to enable the robust self-organization of steady-state mitochondrial distributions, with mitochondria enriched in the distal dendrites and equitably distributed across sister subtrees.

Visual input does not affect mitochondrial movement or localization in HS dendrites

Thus far, our mathematical model and experimental results suggest that dendrite architecture plays a critical role in determining steady-state mitochondrial distribution patterns. However, neuronal activity has been proposed to regulate mitochondrial localization, with local calcium signals arresting mitochondrial motility near active synapses.[19,30] To determine whether neuronal activity regulates mitochondrial localization in HS dendrites, we drove HS activity with a visual stimulus while simultaneously measuring mitochondrial motility in the dendrites. Specifically, we projected the preferred visual stimulus for HS neurons—a global motion stimulus moving from front to back across one eye—on a screen positioned in front of the fly while imaging a genetically encoded calcium reporter (GCaMP6f) and motile mitochondria (mitoDsRed) in distal dendrites (Figures 7A and 7B). The visual stimulus drove robust calcium responses (Figures 7C–7F) but had no effect on mitochondrial speeds, arrest rates, or linear flux rates (Figures 7G–7J). Thus, stimulus-evoked calcium signals do not affect mitochondrial motility in HS dendrites over short timescales.

In principle, visual input could cause a delayed change in mitochondrial transport that we were unable to measure in our *in vivo* imaging experiments. To investigate whether chronic manipulations of neuronal activity affect mitochondrial localization patterns over longer timescales, we prevented activation of HS neurons by rearing flies in continual darkness for 7 days after eclosion. We found, first, that dark rearing had no effect on HS dendrite scaling: regardless of whether the flies were reared in the dark (dark-dark) or under a normal 24 h light-dark cycle (light-dark), HS dendrites obeyed Da Vinci's rule for parent-daughter scaling and sister subtrees scaled with volume proportional to length and trunk thickness proportional to bushiness (Figures S6A–S6E). Next, we measured mitochondrial transport in HS primary dendrites in dark-dark and light-dark flies and found that dark rearing had no effect on mitochondrial speeds, arrest rates, or linear flux rates in primary dendrites (Figures S6F–S6I). Finally, we measured mitochondrial densities in primary and distal HS dendrites and found no differences between dark-dark and light-dark flies (Figures 7K–7M), indicating that visual input is not required for HS neurons to maintain steady-state mitochondrial localization patterns. Instead, our results suggest that mitochondrial distribution patterns are, in effect, hard-wired by the architecture of the dendrite.

DISCUSSION

Neuronal function is inextricably linked to neuronal form.[2–4,6] Our work suggests that maintenance of mitochondrial homeostasis, and specifically the robust self-organization of a specific global mitochondrial distribution pattern, is also linked to neuronal morphology. We present a model in which four simple scaling rules determine mitochondrial localization patterns. Two transport scaling rules— scaling of mitochondrial transport with dendrite radius and proportional splitting of mitochondria at branchpoints—relate local mitochondrial motility rates to dendritic branch radii, and two morphological scaling rules—power law scaling of parent and daughter radii and scaling of trunk thickness with sister subtree size—determine the architecture of the dendrite. There are many possible forms of these dendritic scaling rules, but only a subset of the rules we examined—Da Vinci scaling of parent-daughter radii at branchpoints and sister subtree scaling with trunk thickness proportional to subtree bushiness—predict realistic mitochondrial localization patterns in our model (Figures 6B–6D). Our experimental measurements demonstrate that HS dendrites do in fact obey these morphological scaling rules (Figures 6H–6J). Thus, our work suggests that intracellular transport, and the need to distribute mitochondria throughout elaborately branched dendritic arbors, acts as an important constraint on dendrite morphology.

We have shown that mitochondria are equitably distributed across sister subtrees and enriched in the distal dendrites in HS cells (Figure 1). Distribution of mitochondria throughout the cell is critical for neuronal stability, but the relationship between specific mitochondrial localization patterns (e.g., distal enrichment) and neuronal function is unclear. One possibility is that

indicate model predictions for individual HS dendrite topologies ($N = 26$). Heatmaps show average distal enrichment or sister subtree asymmetry for sister-sister scaling according to $r^2 \sim L/D$ and a range of values for the transport scaling parameter β ($0 \leq \beta \leq 2$) and the parent-daughter scaling parameter α ($1 \leq \alpha \leq 3$). (E and F) HS dendrites labeled by MCFO (E) and associated skeletons and branch radii (F).

(G) Experimental measurements of sister subtree asymmetry with measurements of subtree size including radius, length, depth, bushiness, and volume; asymmetry = $\sqrt{\langle (ST1 - ST2)/(ST1+ST2) \rangle^2}$, averaged over all subtree pairs per cell.

(H–J) Experimental measurements of parent-daughter scaling, with r_0^α plotted versus $r_1^\alpha + r_2^\alpha$ (H, best fit for $\alpha = 2.2$), and sister-sister scaling, with subtree length asymmetry plotted versus subtree volume asymmetry (I) and trunk cross-sectional area asymmetry plotted versus subtree bushiness asymmetry (J). Asymmetry across branchpoints = (ST1 – ST2)/(ST1 + ST2); $N = 649$ branchpoints from 10 neurons from 7 flies. See also Figures S4 and S5.

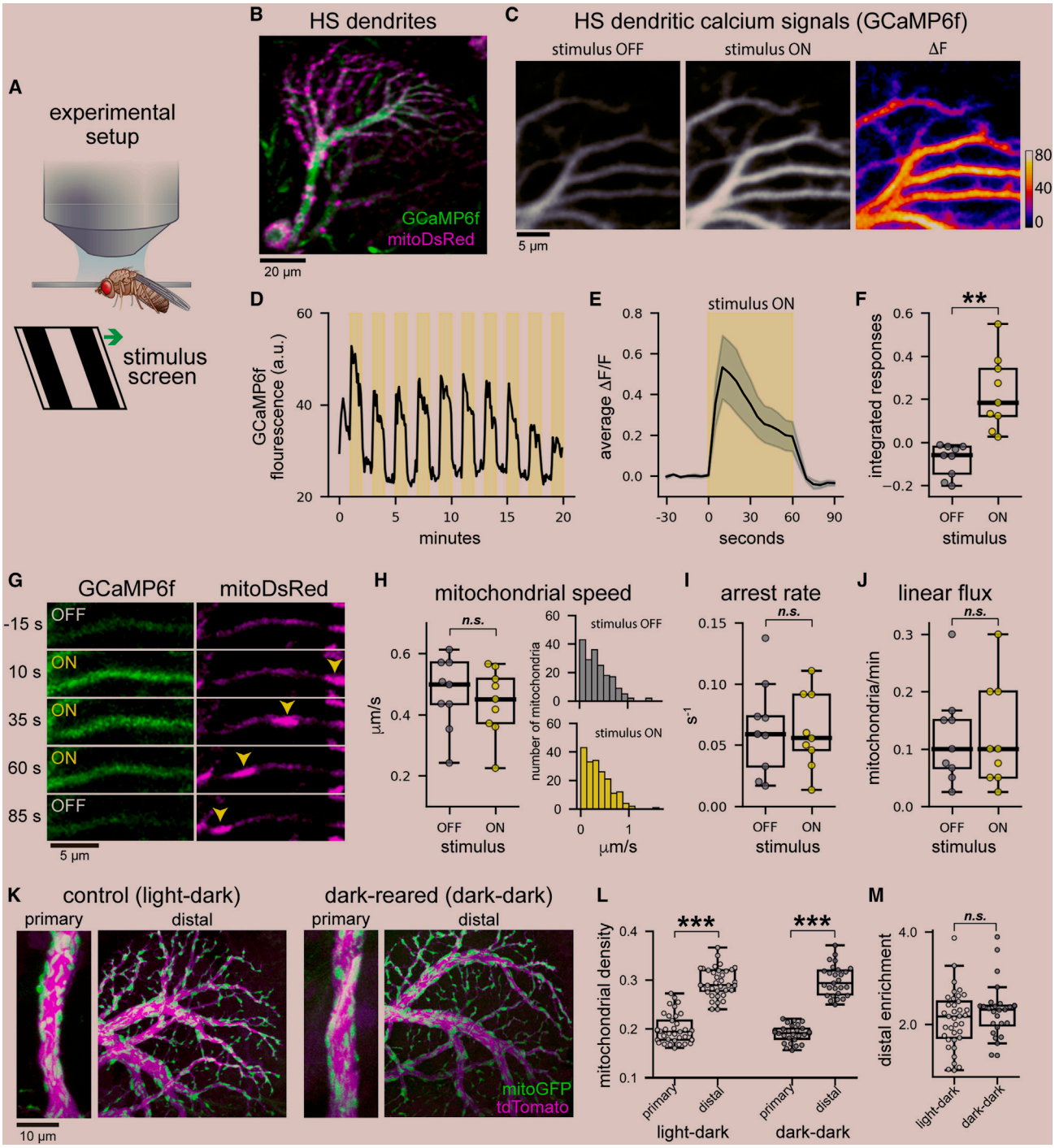

Figure 7. Visual input does not affect mitochondrial movement or localization

(A) Experimental setup: *in vivo* confocal imaging of HS dendrites in head fixed *Drosophila*, with a global motion stimulus (square wave gratings moving in the preferred direction for HS cells (front-to-back) presented on a screen in front of the fly.

(B) HS dendrites, labeled with mitoDsRed (magenta) and GCaMP6f (green), imaged by confocal microscopy while a visual stimulus drove calcium signals in distal HS dendrites.

(C) Images of calcium signals (GCaMP6f) in HS distal dendrites before (stimulus OFF, left column) and during (stimulus ON, center column) visual stimulus presentation. The image on the right shows the difference between the left and center images (ΔF = stimulus ON – stimulus OFF).

(legend continued on next page)

mitochondrial densities simply reflect local energetic demands, with mitochondrial enrichment in subcellular regions that require relatively higher levels of ATP production. The reversal of ion fluxes near synapses is thought to account for a large fraction of the neuron's energy budget,[60,61] and mitochondrial densities weakly correlate with synaptic densities in the dendrites of mouse cortical pyramidal neurons.[50] Mitochondria also buffer calcium,[62] and variations in mitochondrial densities may contribute to compartment-dependent differences in calcium buffering capacities, which have recently been shown to contribute to place field formation in mice.[63]

In addition to supporting dendritic function, enrichment of mitochondria in specific neuronal compartments may play a role in supporting mitochondrial function. In active mitochondria, damaging reactive oxygen species are a by-product of the electron transport chain.[64] Mitochondria compensate for ROS-induced damage by degrading and replacing damaged proteins and by homogenizing the mitochondrial population—diluting damaged proteins and sharing freshly synthesized proteins—via mitochondrial fusion and fission.[65] The majority of mitochondrial proteins are thought to be synthesized and transported into mitochondria in the soma, which are then trafficked to axons and dendrites.[14] Theoretical work suggests that fusion with stationary mitochondria depletes freshly synthesized mitochondrial proteins from motile mitochondria as they move in the anterograde direction.[66] A graded distribution of stationary mitochondria, with higher densities in distal dendrites, may allow neurons to ensure adequate delivery of fresh mitochondrial proteins to distal axons and dendrites while also maximizing complementation across mitochondria in distal compartments. Moreover, mitochondria in HS distal dendrites are large, often spanning multiple dendritic branchpoints (Figure S1C). If young, healthy mitochondria fuse with stationary mitochondria upon arrival in the distal dendrites, passive transport within these elongated mitochondria would ensure uniform local distributions of freshly synthesized mitochondrial proteins. Future versions of our model will include mitochondrial fusion and fission rates, as well as mitochondrial motility.

In our model, equitable distribution of mitochondria across sister subtrees is robust to variation in mitochondrial transport parameters in Da Vinci-scaled dendrites (Figure 6D). Distal enrichment, on the other hand, depends on inverse scaling of motility arrest with dendrite thickness (Figure 6C). The mechanism underlying scaling of motility arrest with branch thickness remains undetermined. In principle, narrowing of dendrite branches, on its own, could be sufficient to increase motility arrest. In cylindrical dendrites, the surface area-to-volume ratio (A_s/V) increases as radius decreases, with $A_s/V \sim 1/r$. Microtubule densities are conserved throughout dendritic arbors[34,35] and the amount of microtubule-based transport should scale with dendrite volume. In contrast, some mechanical interactions that oppose mitochondrial transport should scale with surface area. Friction between motile mitochondria and the cell membrane could oppose motility in thin neuronal processes.[67] Actin localizes to the cell membrane in neurons,[68] and actin-based anchoring opposes microtubule-based transport in several contexts,[69,70] including myosin V-dependent opposition to mitochondrial movement in neurons.[28] Biochemical signals generated at the cell membrane could also contribute to inverse scaling of motility arrest and dendrite radius. High glucose levels trigger mitochondrial arrest in cultured neurons via post-translational modification of the Milton adaptor protein,[71] and quantitative modeling suggests that glucose-mediated motility arrest is sufficient to affect mitochondrial localization patterns.[66] Neurons take up glucose via transporters in the cell membrane[72,73] and, assuming a constant areal density of these transporters, glucose concentrations in the cytosol could increase as the surface area-to-volume ratio increases, thereby promoting increased mitochondrial arrest in thin distal dendrites. In sum, the relative weight of mechanical and biochemical signals generated at the cell membrane versus in the cytosol should increase as neuronal processes narrow, and surface area-to-volume ratios may play a general role in regulating intracellular transport in neurons.

Finally, our results suggest that neuronal signal processing and cell biological requirements may act as competing constraints on neuronal architecture. According to cable theory, Rall's law for parent-daughter scaling is optimal for dendritic signal processing, as it allows for efficient propagation of electrical signals across branchpoints in passive dendrites.[2] However, according to our transport model, Rall's scaling is incompatible with equitable distribution of mitochondria across asymmetrically branched sister subtrees (Figure S5). In contrast, parent-daughter scaling according to Da Vinci's rule facilitates robust equitable distribution of mitochondria for a broad range of transport parameters (Figure 6D). Different neuronal cell types may

(D and E) (D) GCaMP6f signals in the dendritic branch indicated in (C), and average GCaMP6f responses for a population of cells (E) ($\Delta F/F = (F - F_0)/F_0$, where F is GCaMP6f fluorescence and F_0 is the average fluorescence during the 30 s period before stimulus onset); yellow shading indicates when the global motion stimulus was on and gray shading indicates the standard error of the mean.

(F) GCaMP6f signal amplitude when the stimulus was off versus on. GCaMP6f fluorescence was normalized to the median fluorescence for the entire time series (F_m) according to $(F - F_m)/F_m$ and signal amplitudes were calculated by summing the signal for the entire time the stimulus was off or on. The asterisks indicate a significant difference ($p < 0.01$, paired t test, $N = 9$ cells from 9 flies).

(G) Calcium responses to the motion stimulus (GCaMP6f, left) and mitochondria (mitoDsRed, right) in an HS dendritic branch. Yellow arrows indicate a moving mitochondrion.

(H–J) Mitochondrial speeds (H), mitochondrial arrest rates (I), and linear flux rates (J) when the visual stimulus was off or on. Dots overlaid on the boxplots indicate average values for individual flies ($N = 9$ flies). Histograms show the distribution of instantaneous mitochondrial velocities when the stimulus was off (gray, top plot) or on (yellow, bottom plot).

(K) Representative images of mitochondria in HS primary and distal dendrites in flies reared under a normal 24 h light-dark cycle (light-dark) (left) or in continual darkness (dark-dark) (right).

(L and M) Mitochondrial densities in primary and distal HS dendrites in light-dark (open circles) and dark-dark (filled circles) (L) flies and mitochondrial distal enrichment (M). Dots overlaid on the boxplots indicate measurements from individual neurons ($N = 37$ light-dark, 27 dark-dark from >10 flies); asterisks indicate significant differences ($p < 0.001$, unpaired t test). See also Figure S6.

obey different parent-daughter scaling rules depending on the relative weight of signal processing versus cell biological constraints. For example, HS dendrites are not passive,[39] and active dendritic conductances may allow Da Vinci-scaled dendrites to efficiently integrate input signals while also maintaining steady-state mitochondrial localization patterns. In contrast, neurons with purely passive dendrites may be more likely to obey Rall's law and to exhibit inequitable distribution of mitochondria across sister subtrees. Altogether, we argue that a complete set of design principles for dendrite morphology must include rules for the reliable intracellular transport and localization of organelles, in addition to rules governing the integration and propagation of electrical signals. Moreover, maintenance of global mitochondrial distribution patterns is essential for the long-term maintenance of neuronal homeostasis, and neurons that deviate from morphological scaling rules that facilitate equitable distribution of mitochondria, whether due to developmental defects or competing functional constraints on the shape of dendrite, may ultimately be subject to age-related defects in neuronal stability and function.

Limitations of the study

This work sheds light on the relationship between mitochondria dynamics and dendrite architecture. However, it has some limitations. We conducted our experiments using female flies only, and it is possible that there are sex-based differences in dendrite morphology. Moreover, we focused exclusively on *Drosophila* HS neurons, and it remains to be determined if dendrite architecture shapes mitochondrial localization patterns across cell types and species. Finally, our model links mitochondrial transport to dendrite architecture, but additional dynamic processes, including mitochondrial biogenesis, degradation, fission, and fusion, also contribute to the long-term maintenance of a healthy, properly distributed population of mitochondria. We exclude mitochondrial degradation from our model because our experimental measurements suggest that mitophagy in HS dendrites is negligible. In the future, experimental measurements of the spatiotemporal patterns of mitochondrial biogenesis and fission and fusion will be required to constrain a comprehensive quantitative model for mitochondrial homeostasis.

STAR★METHODS

Detailed methods are provided in the online version of this paper and include the following:

- KEY RESOURCES TABLE
- RESOURCE AVAILABILITY
  - Lead contact
  - Materials availability
  - Data and code availability
- EXPERIMENTAL MODEL AND STUDY PARTICIPANT DETAILS
  - *Drosophila* strains and husbandry
- METHOD DETAILS
  - *Drosophila* whole brain dissection and immunostaining
  - *In vivo* imaging
  - Visual stimulus presentation
  - Image analysis
  - Mathematical modeling
- QUANTIFICATION AND STATISTICAL ANALYSIS

SUPPLEMENTAL INFORMATION

Supplemental information can be found online at https://doi.org/10.1016/j.celrep.2024.114190.

ACKNOWLEDGMENTS

We thank Michael Reiser for sharing HS skeletons in the FAFB dataset prior to publication, and we thank Xinnan Wang for providing fly stocks. We are grateful to Tom Clandinin, Alex Mogilner, and all members of the Barnhart lab for comments on the manuscript and helpful discussions. This work was supported by the NIH (R01NS121179 to E.L.B. and F31NS129199 to E.J.D.), the NSF (CAREER award 1848057 to E.F.K. and grant no. 2227609 to E.L.B.), and a UCSD Chancellor Funded Research Grant (to E.F.K.).

AUTHOR CONTRIBUTIONS

Conceptualization, E.L.B. and E.F.K.; methodology, E.L.B., E.J.D., N.L., A.M.L., and J.I.K.; investigation, E.J.D., A.A., N.L., J.I.K., A.M.L., A.J.A., H.Q.W., and E.L.B.; software, A.A., E.F.K., E.L.B., J.K., and N.J.C.; formal analysis, A.A., E.F.K., E.J.D., N.L., J.I.K., and E.L.B.; writing – original draft, E.L.B., E.J.D., A.A., and N.L.; writing – review & editing, E.L.B., E.J.D., E.F.K., A.A., and J.K.; supervision, E.L.B. and E.F.K.

DECLARATION OF INTERESTS

The authors declare no competing interests.

Received: July 17, 2023
Revised: January 8, 2024
Accepted: April 17, 2024

REFERENCES

1. Ramón y Cajal, S. (1995). Histology of the Nervous System of Man and Vertebrates (Oxford University Press).
2. Rall, W. (1959). Branching dendritic trees and motoneuron membrane resistivity. Exp. Neurol. *1*, 491–527. https://doi.org/10.1016/0014-4886(59)90046-9.
3. Mainen, Z.F., and Sejnowski, T.J. (1996). Influence of dendritic structure on firing pattern in model neocortical neurons. Nature *382*, 363–366. https://doi.org/10.1038/382363a0.
4. Vetter, P., Roth, A., and Häusser, M. (2001). Propagation of action potentials in dendrites depends on dendritic morphology. J. Neurophysiol. *85*, 926–937. https://doi.org/10.1152/jn.2001.85.2.926.
5. Wang, S.S.-H., Ambrosini, A.E., and Wittenberg, G.M. (2007). Evolution and Scaling of Dendrites. In Dendrites, G. Stuart, N. Spruston, and M. Hausser, eds. (Oxford University Press).
6. Spruston, N. (2008). Pyramidal neurons: dendritic structure and synaptic integration. Nat. Rev. Neurosci. *9*, 206–221. https://doi.org/10.1038/nrn2286.
7. Cuntz, H., Forstner, F., Borst, A., and Häusser, M. (2010). One rule to grow them all: A general theory of neuronal branching and its practical application. PLoS Comput. Biol. *6*, e1000877. https://doi.org/10.1371/journal.pcbi.1000877.
8. Branco, T., Clark, B.A., and Häusser, M. (2010). Dendritic discrimination of temporal input sequences in cortical neurons. Science *329*, 1671–1675. https://doi.org/10.1126/science.1189664.
9. Sterling, P., and Laughlin, S. (2015). Principles of Neural Design (The MIT Press).
10. Wang, I.E., and Clandinin, T.R. (2016). The influence of wiring economy on nervous system evolution. Curr. Biol. *26*, R1101–R1108. https://doi.org/10.1016/j.cub.2016.08.053.

11. Cuntz, H., Bird, A.D., Mittag, M., Beining, M., Schneider, M., Mediavilla, L., Hoffmann, F.Z., Deller, T., and Jedlicka, P. (2021). A general principle of dendritic constancy: a neuron's size- and shape-invariant excitability. Neuron *109*, 3647–3662.e7. https://doi.org/10.1016/j.neuron.2021.08.028.

12. Menzies, R.A., and Gold, P.H. (1971). The turnover of mitochondria in a variety of tissues of young adult and aged rats. J. Biol. Chem. *246*, 2425–2429.

13. Vincow, E.S., Merrihew, G., Thomas, R.E., Shulman, N.J., Beyer, R.P., MacCoss, M.J., and Pallanck, L.J. (2013). The PINK1-Parkin pathway promotes both mitophagy and selective respiratory chain turnover in vivo. Proc. Natl. Acad. Sci. USA *110*, 6400–6405. https://doi.org/10.1073/pnas.1221132110.

14. Misgeld, T., and Schwarz, T.L. (2017). Mitostasis in neurons: maintaining mitochondria in an extended cellular architecture. Neuron *96*, 651–666. https://doi.org/10.1016/j.neuron.2017.09.055.

15. Sartori, F., Hafner, A.S., Karimi, A., Nold, A., Fonkeu, Y., Schuman, E.M., and Tchumatchenko, T. (2020). Statistical laws of protein motion in neuronal dendritic trees. Cell Rep. *33*, 108391. https://doi.org/10.1016/j.celrep.2020.108391.

16. Liao, M., Liang, X., and Howard, J. (2021). The narrowing of dendrite branches across nodes follows a well-defined scaling law. Proc. Natl. Acad. Sci. USA *118*, e2022395118. https://doi.org/10.1073/pnas.2022395118.

17. Morris, R.L., and Hollenbeck, P.J. (1995). Axonal transport of mitochondria along microtubules and F-actin in living vertebrate neurons. J. Cell Biol. *131*, 1315–1326. https://doi.org/10.1083/jcb.131.5.1315.

18. Overly, C.C., Rieff, H.I., and Hollenbeck, P.J. (1996). Organelle motility and metabolism in axons vs dendrites of cultured hippocampal neurons. J. Cell Sci. *109*, 971–980. https://doi.org/10.1242/jcs.109.5.971.

19. Wang, X., and Schwarz, T.L. (2009). The mechanism of Ca2+ -dependent regulation of kinesin-mediated mitochondrial motility. Cell *136*, 163–174. https://doi.org/10.1016/j.cell.2008.11.046.

20. Saxton, W.M., and Hollenbeck, P.J. (2012). The axonal transport of mitochondria. J. Cell Sci. *125*, 2095–2104. https://doi.org/10.1242/jcs.053850.

21. Plucińska, G., Paquet, D., Hruscha, A., Godinho, L., Haass, C., Schmid, B., and Misgeld, T. (2012). In vivo imaging of disease-related mitochondrial dynamics in a vertebrate model system. J. Neurosci. *32*, 16203–16212. https://doi.org/10.1523/jneurosci.1327-12.2012.

22. Mandal, A., Wong, H.T.C., Pinter, K., Mosqueda, N., Beirl, A., Lomash, R.M., Won, S., Kindt, K.S., and Drerup, C.M. (2021). Retrograde mitochondrial transport Is essential for organelle distribution and health in zebrafish neurons. J. Neurosci. *41*, 1371–1392. https://doi.org/10.1523/jneurosci.1316-20.2020.

23. Silva, C.A., Yalnizyan-Carson, A., Fernández Busch, M.V., van Zwieten, M., Verhage, M., and Lohmann, C. (2021). Activity-dependent regulation of mitochondrial motility in developing cortical dendrites. Elife *10*, e62091. https://doi.org/10.7554/eLife.62091.

24. Vagnoni, A., and Bullock, S.L. (2018). A cAMP/PKA/Kinesin-1 axis promotes the axonal transport of mitochondria in aging Drosophila neurons. Curr. Biol. *28*, 1265–1272.e4. https://doi.org/10.1016/j.cub.2018.02.048.

25. Barnhart, E.L. (2016). Mechanics of mitochondrial motility in neurons. Curr. Opin. Cell Biol. *38*, 90–99. https://doi.org/10.1016/j.ceb.2016.02.022.

26. Pilling, A.D., Horiuchi, D., Lively, C.M., and Saxton, W.M. (2006). Kinesin-1 and Dynein are the primary motors for fast transport of mitochondria in Drosophila motor axons. Mol. Biol. Cell *17*, 2057–2068. https://doi.org/10.1091/mbc.e05-06-0526.

27. Kang, J.S., Tian, J.H., Pan, P.Y., Zald, P., Li, C., Deng, C., and Sheng, Z.H. (2008). Docking of axonal mitochondria by syntaphilin controls their mobility and affects short-term facilitation. Cell *132*, 137–148. https://doi.org/10.1016/j.cell.2007.11.024.

28. Pathak, D., Sepp, K.J., and Hollenbeck, P.J. (2010). Evidence that myosin activity opposes microtubule-based axonal transport of mitochondria. J. Neurosci. *30*, 8984–8992. https://doi.org/10.1523/jneurosci.1621-10.2010.

29. Schwarz, T.L. (2013). Mitochondrial trafficking in neurons. Cold Spring Harbor Perspect. Biol. *5*, a011304. https://doi.org/10.1101/cshperspect.a011304.

30. MacAskill, A.F., Rinholm, J.E., Twelvetrees, A.E., Arancibia-Carcamo, I.L., Muir, J., Fransson, A., Aspenstrom, P., Attwell, D., and Kittler, J.T. (2009). Miro1 Is a calcium sensor for glutamate receptor-dependent localization of mitochondria at synapses. Neuron *61*, 541–555. https://doi.org/10.1016/j.neuron.2009.01.030.

31. Li, S., Xiong, G.J., Huang, N., and Sheng, Z.H. (2020). The cross-talk of energy sensing and mitochondrial anchoring sustains synaptic efficacy by maintaining presynaptic metabolism. Nat. Metab. *2*, 1077–1095. https://doi.org/10.1038/s42255-020-00289-0.

32. Smit-Rigter, L., Rajendran, R., Silva, C.A.P., Spierenburg, L., Groeneweg, F., Ruimschotel, E.M., van Versendaal, D., van der Togt, C., Eysel, U.T., Heimel, J.A., et al. (2016). Mitochondrial dynamics in visual cortex are limited in vivo and not affected by axonal structural plasticity. Curr. Biol. *26*, 2609–2616. https://doi.org/10.1016/j.cub.2016.07.033.

33. Faits, M.C., Zhang, C., Soto, F., and Kerschensteiner, D. (2016). Dendritic mitochondria reach stable positions during circuit development. Elife *5*, e11583. https://doi.org/10.7554/eLife.11583.

34. Kubota, Y., Karube, F., Nomura, M., Gulledge, A.T., Mochizuki, A., Schertel, A., and Kawaguchi, Y. (2011). Conserved properties of dendritic trees in four cortical interneuron subtypes. Sci. Rep. *1*, 89. https://doi.org/10.1038/srep00089.

35. Katrukha, E.A., Jurriens, D., Salas Pastene, D.M., and Kapitein, L.C. (2021). Quantitative mapping of dense microtubule arrays in mammalian neurons. Elife *10*, e67925. https://doi.org/10.7554/eLife.67925.

36. Hausen, K. (1982). Motion sensitive interneurons in the optomotor system of the fly, part II. The horizontal cells: receptive-field organization and response characteristics. Biol. Cybern. *46*, 67–79. https://doi.org/10.1007/Bf00335352.

37. Krapp, H.G., Hengstenberg, B., and Hengstenberg, R. (1998). Dendritic structure and receptive-field organization of optic flow processing interneurons in the fly. J. Neurophysiol. *79*, 1902–1917. https://doi.org/10.1152/jn.1998.79.4.1902.

38. Scott, E.K., Raabe, T., and Luo, L. (2002). Structure of the vertical and horizontal system neurons of the lobula plate in Drosophila. J. Comp. Neurol. *454*, 470–481. https://doi.org/10.1002/cne.10467.

39. Schnell, B., Joesch, M., Forstner, F., Raghu, S.V., Otsuna, H., Ito, K., Borst, A., and Reiff, D.F. (2010). Processing of horizontal optic flow in three visual interneurons of the Drosophila brain. J. Neurophysiol. *103*, 1646–1657. https://doi.org/10.1152/jn.00950.2009.

40. Fujiwara, T., Cruz, T.L., Bohnslav, J.P., and Chiappe, M.E. (2017). A faithful internal representation of walking movements in the Drosophila visual system. Nat. Neurosci. *20*, 72–81. https://doi.org/10.1038/nn.4435.

41. Kim, A.J., Fenk, L.M., Lyu, C., and Maimon, G. (2017). Quantitative predictions orchestrate visual signaling in Drosophila. Cell *168*, 280–294.e12. https://doi.org/10.1016/j.cell.2016.12.005.

42. Barnhart, E.L., Wang, I.E., Wei, H., Desplan, C., and Clandinin, T.R. (2018). Sequential nonlinear filtering of local motion cues by global motion circuits. Neuron *100*, 229–243.e3. https://doi.org/10.1016/j.neuron.2018.08.022.

43. Maisak, M.S., Haag, J., Ammer, G., Serbe, E., Meier, M., Leonhardt, A., Schilling, T., Bahl, A., Rubin, G.M., Nern, A., et al. (2013). A directional tuning map of Drosophila elementary motion detectors. Nature *500*, 212–216. https://doi.org/10.1038/nature12320.

44. Cuntz, H., Borst, A., and Segev, I. (2007). Optimization principles of dendritic structure. Theor. Biol. Med. Model. *4*, 21. https://doi.org/10.1186/1742-4682-4-21.

45. Cuntz, H., Forstner, F., Haag, J., and Borst, A. (2008). The morphological identity of insect dendrites. PLoS Comput. Biol. *4*, e1000251. https://doi.org/10.1371/journal.pcbi.1000251.

46. Cuntz, H., Forstner, F., Schnell, B., Ammer, G., Raghu, S.V., and Borst, A. (2013). Preserving neural function under extreme scaling. PLoS One *8*, e71540. https://doi.org/10.1371/journal.pone.0071540.

47. Zheng, Z., Lauritzen, J.S., Perlman, E., Robinson, C.G., Nichols, M., Milkie, D., Torrens, O., Price, J., Fisher, C.B., Sharifi, N., et al. (2018). A complete electron microscopy volume of the drain of adult Drosophila melanogaster. Cell *174*, 730–743.e722. https://doi.org/10.1016/j.cell.2018.06.019.

48. Zhao, A., Nern, A., Koskela, S., Dreher, M., Erginkaya, M., Laughland, C.W., Ludwigh, H., Thomson, A., Hoeller, J., Parekh, R., et al. (2023). A comprehensive neuroanatomical survey of the Drosophila Lobula Plate Tangential Neurons with predictions for their optic flow sensitivity. Preprint at bioRxiv. https://doi.org/10.1101/2023.10.16.562634.

49. Popov, V., Medvedev, N.I., Davies, H.A., and Stewart, M.G. (2005). Mitochondria form a filamentous reticular network in hippocampal dendrites but are present as discrete bodies in axons: a three-dimensional ultrastructural study. J. Comp. Neurol. *492*, 50–65. https://doi.org/10.1002/cne.20682.

50. Turner, N.L., Macrina, T., Bae, J.A., Yang, R., Wilson, A.M., Schneider-Mizell, C., Lee, K., Lu, R., Wu, J., Bodor, A.L., et al. (2022). Reconstruction of neocortex: Organelles, compartments, cells, circuits, and activity. Cell *185*, 1082–1100.e24. https://doi.org/10.1016/j.cell.2022.01.023.

51. Lewis, T.L., Jr., Turi, G.F., Kwon, S.K., Losonczy, A., and Polleux, F. (2016). Progressive decrease of mitochondrial motility during maturation of cortical axons in vitro and in vivo. Curr. Biol. *26*, 2602–2608. https://doi.org/10.1016/j.cub.2016.07.064.

52. McWilliams, T.G., Prescott, A.R., Allen, G.F.G., Tamjar, J., Munson, M.J., Thomson, C., Muqit, M.M.K., and Ganley, I.G. (2016). mito-QC illuminates mitophagy and mitochondrial architecture in vivo. J. Cell Biol. *214*, 333–345. https://doi.org/10.1083/jcb.201603039.

53. Cason, S.E., Mogre, S.S., Holzbaur, E.L.F., and Koslover, E.F. (2022). Spatiotemporal analysis of axonal autophagosome-lysosome dynamics reveals limited fusion events and slow maturation. Mol. Biol. Cell *33*, ar123. https://doi.org/10.1091/mbc.E22-03-0111.

54. Cherniak, C., Changizi, M., and Kang, D. (1999). Large-scale optimization of neuron arbors. Phys. Rev. E *59*, 6001–6009. https://doi.org/10.1103/physreve.59.6001.

55. Chklovskii, D.B., and Stepanyants, A. (2003). Power-law for axon diameters at branch point. BMC Neurosci. *4*, 18. https://doi.org/10.1186/1471-2202-4-18.

56. Hillman, D.E. (1979). Neuronal Shape Parameters and Substructures as a Basis of Neuronal Form (MIT Press).

57. Murray, C.D. (1926). The physiological principle of minimum work applied to the angle of branching of arteries. J. Gen. Physiol. *9*, 835–841. https://doi.org/10.1085/jgp.9.6.835.

58. Leonardo; Richter, J.P., and Bell, R.C. (1970). The notebooks of Leonardo da Vinci (Dover Publications).

59. Nern, A., Pfeiffer, B.D., and Rubin, G.M. (2015). Optimized tools for multicolor stochastic labeling reveal diverse stereotyped cell arrangements in the fly visual system. Proc. Natl. Acad. Sci. USA *112*, E2967–E2976. https://doi.org/10.1073/pnas.1506763112.

60. Attwell, D., and Laughlin, S.B. (2001). An energy budget for signaling in the grey matter of the brain. J. Cerebr. Blood Flow Metabol. *21*, 1133–1145. https://doi.org/10.1097/00004647-200110000-00001.

61. Harris, J.J., Jolivet, R., and Attwell, D. (2012). Synaptic energy use and supply. Neuron *75*, 762–777. https://doi.org/10.1016/j.neuron.2012.08.019.

62. Werth, J.L., and Thayer, S.A. (1994). Mitochondria buffer physiological calcium loads in cultured rat dorsal root ganglion neurons. J. Neurosci. *14*, 348–356. https://doi.org/10.1523/jneurosci.14-01-00348.1994.

63. O'Hare, J.K., Gonzalez, K.C., Herrlinger, S.A., Hirabayashi, Y., Hewitt, V.L., Blockus, H., Szoboszlay, M., Rolotti, S.V., Geiller, T.C., Negrean, A., et al. (2022). Compartment-specific tuning of dendritic feature selectivity by intracellular Ca(2+) release. Science *375*, eabm1670. https://doi.org/10.1126/science.abm1670.

64. Miwa, S., and Brand, M.D. (2003). Mitochondrial matrix reactive oxygen species production is very sensitive to mild uncoupling. Biochem. Soc. Trans. *31*, 1300–1301. https://doi.org/10.1042/bst0311300.

65. Youle, R.J., and van der Bliek, A.M. (2012). Mitochondrial fission, fusion, and stress. Science *337*, 1062–1065. https://doi.org/10.1126/science.1219855.

66. Agrawal, A., and Koslover, E.F. (2021). Optimizing mitochondrial maintenance in extended neuronal projections. PLoS Comput. Biol. *17*, e1009073. https://doi.org/10.1371/journal.pcbi.1009073.

67. Narayanareddy, B.R.J., Vartiainen, S., Hariri, N., O'Dowd, D.K., and Gross, S.P. (2014). A biophysical analysis of mitochondrial movement: differences between transport in neuronal cell bodies versus processes. Traffic *15*, 762–771. https://doi.org/10.1111/tra.12171.

68. Leiss, F., Koper, E., Hein, I., Fouquet, W., Lindner, J., Sigrist, S., and Tavosanis, G. (2009). Characterization of dendritic spines in the Drosophila central nervous system. Dev. Neurobiol. *69*, 221–234. https://doi.org/10.1002/dneu.20699.

69. Kapitein, L.C., van Bergeijk, P., Lipka, J., Keijzer, N., Wulf, P.S., Katrukha, E.A., Akhmanova, A., and Hoogenraad, C.C. (2013). Myosin-V opposes microtubule-based cargo transport and drives directional motility on cortical actin. Curr. Biol. *23*, 828–834. https://doi.org/10.1016/j.cub.2013.03.068.

70. Lu, W., Lakonishok, M., Liu, R., Billington, N., Rich, A., Glotzer, M., Sellers, J.R., and Gelfand, V.I. (2020). Competition between kinesin-1 and myosin-V defines Drosophila posterior determination. Elife *9*, e54216. https://doi.org/10.7554/eLife.54216.

71. Pekkurnaz, G., Trinidad, J.C., Wang, X., Kong, D., and Schwarz, T.L. (2014). Glucose regulates mitochondrial motility via Milton modification by O-GlcNAc transferase. Cell *158*, 54–68. https://doi.org/10.1016/j.cell.2014.06.007.

72. Ferreira, J.M., Burnett, A.L., and Rameau, G.A. (2011). Activity-dependent regulation of surface glucose transporter-3. J. Neurosci. *31*, 1991–1999. https://doi.org/10.1523/jneurosci.1850-09.2011.

73. Lundgaard, I., Li, B., Xie, L., Kang, H., Sanggaard, S., Haswell, J.D.R., Sun, W., Goldman, S., Blekot, S., Nielsen, M., et al. (2015). Direct neuronal glucose uptake heralds activity-dependent increases in cerebral metabolism. Nat. Commun. *6*, 6807. https://doi.org/10.1038/ncomms7807.

74. Schindelin, J., Arganda-Carreras, I., Frise, E., Kaynig, V., Longair, M., Pietzsch, T., Preibisch, S., Rueden, C., Saalfeld, S., Schmid, B., et al. (2012). Fiji: an open-source platform for biological-image analysis. Nat. Methods *9*, 676–682. https://doi.org/10.1038/nmeth.2019.

75. Berg, S., Kutra, D., Kroeger, T., Straehle, C.N., Kausler, B.X., Haubold, C., Schiegg, M., Ales, J., Beier, T., Rudy, M., et al. (2019). ilastik: interactive machine learning for (bio)image analysis. Nat. Methods *16*, 1226–1232. https://doi.org/10.1038/s41592-019-0582-9.

76. Feng, L., Zhao, T., and Kim, J. (2015). neuTube 1.0: A new design for efficient neuron reconstruction software based on the SWC format. eNeuro *2*, ENEURO.0049-14.2014. https://doi.org/10.1523/eneuro.0049-14.2014.

77. Cardona, A., Saalfeld, S., Schindelin, J., Arganda-Carreras, I., Preibisch, S., Longair, M., Tomancak, P., Hartenstein, V., and Douglas, R.J. (2012). TrakEM2 software for neural circuit reconstruction. PLoS One *7*, e38011. https://doi.org/10.1371/journal.pone.0038011.

78. Peirce, J., Gray, J.R., Simpson, S., MacAskill, M., Höchenberger, R., Sogo, H., Kastman, E., and Lindeløv, J.K. (2019). PsychoPy2: Experiments in behavior made easy. Behav. Res. Methods *51*, 195–203. https://doi.org/10.3758/s13428-018-01193-y.

79. Thévenaz, P., Ruttimann, U.E., and Unser, M. (1998). A pyramid approach to subpixel registration based on intensity. IEEE Trans. Image Process. *7*, 27–41. https://doi.org/10.1109/83.650848.

STAR★METHODS

KEY RESOURCES TABLE

REAGENT or RESOURCE	SOURCE	IDENTIFIER
Antibodies		
Mouse monoclonal anti-BRP	DSHB	nc-82; RRID: AB_2314866
Rabbit monoclonal anti-HA	Cell Signaling Technology	3724; RRID: AB_10693385
DyLight 550 Mouse monoclonal anti-V5	Bio-Rad	MCA1360D550GA; RRID: AB_2687576
Rat monoclonal anti-FLAG	Novus Biologicals	NBP1-06712; RRID: AB_1625981
Chicken polyclonal anti-GFP	Aves Labs	GFP-1010; RRID: AB_2307313
Rabbit polyclonal anti-RFP	Rockland	600-401-379; RRID: AB_2209751
Alexa Fluor 405 Goat anti-Mouse IgG	Thermo Fisher Scientific	A-31553; RRID: AB_221604
Alexa Fluor Plus 488 Donkey anti-Rabbit IgG	Thermo Fisher Scientific	A-32790; RRID: AB_2762833
Alexa Fluor 488 Goat anti-Chicken IgY	Thermo Fisher Scientific	A-11039; RRID: AB_2534096
Alexa Fluor 555 Goat anti-Rabbit IgG	Thermo Fisher Scientific	A-21428; RRID: AB_2535849
Alexa Fluor 647 Donkey anti-Rat IgG	Abcam	ab150155; RRID: AB_2813835
Alexa Fluor 647 Goat anti-Mouse IgG	Thermo Fisher Scientific	A-21235; RRID: AB_2535804
Chemicals, peptides, and recombinant proteins		
Bondic UV glue	BONDIC	N/A
ProLong™ Gold Antifade Mountant	Invitrogen	P10144
paraformaldehyde	Sigma-Aldrich	158127
Triton X-100	Sigma-Aldrich	T9284
Experimental models: Organisms/strains		
Canton-S	Bloomington Stock Center	64349
w-; +; R27B03-GAL4 (HS)	Bloomington Stock Center	49211
w-; UAS-GCaMP6f; +	Bloomington Stock Center	52869
w+; UAS-mitoDsRed; +	Xinnan Wang	N/A
w+; UAS-mitoGFP; +	Xinnan Wang	N/A
w+; UAS-tdTomato; +	Bloomington Stock Center	36327
w+; UAS-mitoGFP,UAS-tdTomato/CyO; R27B03-GAL4(HS)/TM6B	this study	N/A
w-,hs-FLPG5; +; 10xUAS(FRT.stop) myr:smGdP-HA,10xUAS(FRT.stop) myr:smGdP-V5-THS-10xUAS(FRT.stop) myr:smGdP-FLAG (MCFO stock)	Bloomington Stock Center	64085
w+; UAS-mitoQC; +	Bloomington Stock Center	91640
Software and algorithms		
MATLAB	MathWorks	https://www.mathworks.com/
Fiji	Schindelin et al.[74]	https://fiji.sc/
Python 3	Python	https://www.anaconda.com/products/distribution
ilastik	Berg et al.[75]	https://www.ilastik.org/
neuTube	Feng et al.[76]	https://neutracing.com/
TREES toolbox	Cuntz et al.[7]	https://www.treestoolbox.org/
TrakEM2 Fiji plug-in	Cardona et al.[77]	https://imagej.net/plugins/trakem2/
PsychoPy	Peirce et al.[78]	https://www.psychopy.org/

(*Continued on next page*)

Continued

REAGENT or RESOURCE	SOURCE	IDENTIFIER
Custom written Python code for quantifying mitochondrial transport, extracting visual stimulus-driven calcium signals from *in vivo* images, and generating synthetic dendritic skeletons	this paper	https://zenodo.org/records/10777759
Custom written MATLAB code for modeling mitochondrial localization patterns in branched dendrites	this paper	https://zenodo.org/records/10777759

RESOURCE AVAILABILITY

Lead contact

Further information and reasonable requests for resources and reagents should be directed to the lead contact, Erin Barnhart (eb3305@columbia.edu).

Materials availability

The w+; UAS-mitoGFP,UAS-tdTomato/CyO; R27B03-GAL4(HS)/TM6B *Drosophila* stock will be made available by the lead contact upon request.

Data and code availability

- Data will be made available by the lead contact upon request.
- Custom written code is available online: https://zenodo.org/records/10777759.
- Any additional information required to reanalyze the data reported in this work is available from the lead contact upon request.

EXPERIMENTAL MODEL AND STUDY PARTICIPANT DETAILS

Drosophila strains and husbandry

Drosophila stocks used in this study include wild-type Canton S (BSC64349), R27B03-GAL4 (HS driver, BSC49211), UAS-GCaMP6f (BSC52869), MCFO-1 (BSC64085), UAS-tdTomato (BSC36327), UAS-mitoQC (BSC91640), and UAS-mitoDsRed and UAS-mitoGFP (gifts from Xinnan Wang). The w+; UAS-mitoGFP,UAS-tdTomato/CyO; R27B03-GAL4(HS)/TM6B stock was generated by recombining UAS-tdTomato and UAS-mitoGFP on the second chromosome. All flies were cultured in vials containing a standard cornmeal-agar medium at 25°C with 60% humidity in a 12h light/dark cycle. Crosses were flipped into fresh vials every 3 days and progeny were imaged 4–7 days after eclosion.

METHOD DETAILS

Drosophila whole brain dissection and immunostaining

For mitochondria labeling, female flies were collected 1–2 days after eclosion and then dissected 3–5 days later. Flies were anesthetized on ice before dissection in 2% paraformaldehyde and 0.1 M L-Lysine on an elastomer plate, followed by fixation for 1 h on ice. Samples were washed three times (5 min per wash) with PBST (PBS with 0.5% Triton), blocked in PBST-NGS (PBST with 5% normal goat serum, Abcam) for 30 min at room temperature, and incubated for two nights at 4C in primary antibodies diluted in PBST-NGS (Chicken anti-GFP, 1:1000 dilution; Rabbit anti-RFP, 1:100; and Mouse anti-BRP, 1:10). Then, brains were washed three times (30 min per wash) in PBST-NGS before incubation in secondary antibodies (AF488 Goat anti-Chicken, 1:1000; AF555 Goat anti-Rabbit, 1:500; and AF647 Goat anti-Mouse, 1:500) for 3 h at room temperature. Finally, brains were washed three times (20 min per wash) in PBST-NGS prior to mounting in ProLong gold antifade (Invitrogen).

For MultiColor FlpOut (MCFO) labeling, HS GAL4 driver lines were crossed with MCFO[59] virgins. Offspring were collected 1–2 days after eclosion, heat shocked at 38°C for 25 min, and dissected three days later. Fly brains were dissected in cold PBS solution and fixed in 4% formaldehyde for 25 min at room temperature. Brains were subsequently rinsed with PBST and blocked in PBST-NGS at room temperature for 1.5 h. Brains were incubated for two nights in primary antibodies diluted in PBST-NGS (Mouse anti-BRP, 1:10; Rabbit anti-HA, 1:400; and Rat anti-FLAG, 1:200), incubated for two nights in secondary antibodies in PBST-NGS (AF405 Goat anti-Mouse, 1:50; AF488 Donkey anti-Rabbit, 1:400; and AF647 Donkey anti-Rat, 1:200), and finally incubated overnight in tertiary antibodies in PBST-NGS (DyLight550 Mouse anti-V5, 1:300). Prior to each antibody incubation, brains were washed three times for 10 min each in PBST. All antibody incubations were performed at 4°C. Brains were mounted in VectaShield (Vector Laboratories) and imaged using a confocal microscope.

In vivo imaging

Female flies were cold anesthetized and positioned in a key-hole cut in a thin metal shim, with the back of the head exposed above the shim and the eyes below the shim. The fly was secured in place with UV-cured glue (Bondic) and the brain was exposed using fine forceps to dissect a hole in the cuticle and remove overlying fat and trachea. The brain was perfused with a sugar saline solution (103 mM NaCl, 3 mM KCl, 5 mM TES, 1 mM NaH_2PO_4, 26 mM $NaHCO_2$, 4 mM $MgCl_2$, 1.5 mM $CaCl_2$, 10 mM trehalose, 10 mM glucose, and 7 mM sucrose). Neurons were imaged using an integrated confocal and two-photon microscope (Leica SP8 CSU MP Dual) equipped with a 25×1.0 NA water immersion objective (Leica). For confocal imaging of motile mitochondria (Figures 2, 4A–4G, 5, and 7G–7J), stationary GFP- or DsRed-tagged mitochondria in the field of view were photobleached prior to time lapse imaging, allowing for resolution of individual motile mitochondria as they moved through the field of view. In distal dendrites, bleaching stationary mitochondria prevented reliable imaging of mitochondria moving in the retrograde direction, so all subsequent analysis was conducted for anterograde mitochondria only. Confocal z-stacks (voxel size = 108.54 nm × 108.54 nm x 1 μm) were collected over time (frame rates ranged from 1 to 5 s per z stack, depending on the experiment) for 10–20 min after photobleaching.

Visual stimulus presentation

Visual stimuli were generated using PsychoPy[78] (Python) and presented on a white screen (Da-Lite Dual-Vision vinyl, AV Outlet) using a digital light projector (DLP LightCrafter, Texas Instruments). The stimulus screen spanned ∼60° of the fly's visual field horizontally and ∼60° vertically, and the stimulus was updated at 60 Hz. To avoid detection of light from the stimulus by the microscope, the stimulus was filtered using a 472/30 nm bandpass filter (Semrock). Voltage signals from the imaging software were relayed to PsychoPy via a LabJack device, in order to synchronize the stimulus and the imaging frames. The visual stimuli were full contrast square wave gratings (λ = 30°) that filled the entire stimulus screen. When the stimulus was on, the gratings moved in the preferred direction for HS neurons (front-to-back across one eye) at 30°/s; when the stimulus was off, the gratings remained stationary.

Image analysis

Quantification of mitochondrial morphologies and localization patterns

Mitochondrial densities were measured from confocal z-stacks of HS neurons labeled with mitoGFP and tdTomato and from ssTEM images from the Female Adult Fly Brain (FAFB) dataset.[47] For confocal images, the dendrite (cytosolic tdTomato) and the mitochondria within it (mitoGFP) were manually segmented from three to six z slices per primary or distal dendrite using Fiji. Densities were calculated as D = M/(M + C), where M is the total number pixels segmented from the mitoGFP channel and C is the total number of pixels segmented from the cytosolic tdTomato channel. Analysis of mitochondrial densities in light-dark and dark-dark samples (Figure 7K–7M) was conducted in a blinded fashion: images were de-identified and randomized prior to z slices selection and manual segmentation. For ssTEM images from the FAFB dataset,[47] HS neurons were identified within the larger FAFB image volume using previously traced HS skeletons.[48] To measure the size of individual mitochondria, small image volumes centered around HS dendritic segments were cropped out of the FAFB dataset, and mitochondria within HS dendrites were manually segmented in three dimensions using the TrakEM2 Fiji plug-in.[77] To measure mitochondrial localization patterns throughout HS neurons, all HS skeletons were resampled using a python-CATMAID interface library, pymaid, such that the graph distance between skeleton nodes was 5 μm. All branch points and endpoints were preserved during resampling. Two-dimensional image slices centered around each node in the resampled skeleton were then cropped out of the FAFB dataset, and HS neurons and the mitochondria within them were manually segmented in each image using TrakEM. Mitochondrial density (total mitochondrial area/total neurite area) was measured as a function of neuronal compartment (axons versus dendrites), distance from the soma, and across sister subtree pairs using custom-written Python code.

Quantification of mitochondrial motility

Mitochondrial lengths, speeds, arrest rates, and flux rates were measured from maximum projections of confocal z-stacks of mitoGFP and cytosolic tdTomato expressed in HS neurons. Max projections were aligned using the TurboReg[79] Fiji plugin. Linear mitochondrial flux rates were measured by counting the number of motile mitochondria that moved through a particular cross-section of a dendritic branch in either the anterograde or retrograde direction per unit time. Individual motile mitochondria were hand-tracked to generate mitochondrial tracks using the Tracking Fiji built in plugin. Mitochondrial speeds and arrest rates were measured from these mitochondrial tracks using custom-written Python code. Mitochondrial speeds were calculated for each mitochondrion as an average speed (distance over time) above an instantaneous speed threshold of 0.1 μm/s. Arrest rates were measured for each motile mitochondrion by counting the number of times the mitochondrion stopped moving for the entire time period it was tracked. The arrest rate (stops per second) was then calculated by dividing the total number of stops by the total time. Lengths of motile mitochondria were measured using the line selection tool in Fiji.

Estimates of mitochondrial exchange rate and motile fraction

A mitochondrial volume exchange rate J was estimated based on experimental measurements of mitochondrial linear flux ($\rho \sim 2$ mitochondria/minute, Figure 2H) and the approximate volume of the motile mitochondria ($V_m \sim 0.5\ \mu m^3$): $J = \rho V_m \sim 1\ \mu m^3$/min. The average volume of motile mitochondria was estimated as $V_m = \pi r^2 l$, where l is the length of a motile mitochondrion (∼2 μm, Figure 2E) and r is the radius (assumed to be ∼0.3 μm). $V_m \sim 0.5\ \mu m^3$ is consistent with the median mitochondrial volume in our EM reconstructions (Figure S1C). The fraction of the total mitochondrial volume in the entire dendritic arbor exchanged through the primary dendrite per hour was estimated based on experimental measurements of the mitochondrial density in the entire dendrite

(c ~ 20%, Figure S1F), previously published measurements of the total volume of the dendrite (V_d ~2000 μm^3),[46] and the mitochondrial volume exchange rate (J ~ 1 μm^3/min): $J_{norm} = J/(c\ V_d)$ ~ 15% hr^{-1}. The fraction of mitochondria that are motile in the primary dendrite at any given instant was estimated based on the mitochondrial volume exchange rate (J ~ 1 μm^3/min), the typical speed of motile mitochondria (v ~ 0.6 μm/s, Figure 2F), the mitochondrial volume density (c ~ 10% in the primary dendrite, Figure S1G), and the cross-sectional area (A_d ~ 30 μm^2, estimated from the radius of the primary dendrite, r ~ 3 μm, Figure 2D): $f_m = 2\ J/(v\ c\ A_d) \sim 2\%$.

Quantification of mitophagy

Confocal z-stacks of HS dendrites and cell bodies, acquired via *in vivo* confocal imaging of head-fixed flies, were cropped into substacks containing distinct subcellular compartments (soma, primary dendrite, and distal dendrites). Mitolysosomes (red-only voxels) and mitochondria (red+green voxels) in each substack were manually segmented in Fiji to create binary masks, and the mitophagy index (MI) was calculated as MI = (number of mitolysosomes voxels)/(number of mitochondria voxels) for a given compartment.

Quantification of dendritic branching patterns

Dendritic arbors for individual HS neurons were segmented from MCFO images using ilastik[75] and custom-written Python code. Unique pixel classifiers were trained in ilastik for each MCFO z stack, and binary masks were generated from the resulting probability maps in Python by thresholding and connected component analysis. Binary masks were then manually cleaned up in Fiji and skeletonized using the Skeletonize (2D/3D) Fiji built in plugin. Dendritic arbors for light-dark and dark-dark were randomized and manually traced using 3D images of a cytosolic volume marker, tdTomato, using neuTube[76] and custom-written MATLAB code. Skeleton data was translated into a set of nodes (including junction nodes, parent node, and distal tips) with three-dimensional coordinates, and curved edge paths connecting the nodes. Once the initial network structure was extracted, manual clean-up was carried out with a custom MATLAB GUI, involving the removal of short spurious branches ('shrubs') from the network. A combination of percentile and asymmetry cutoffs were used to quantitatively remove shrubs that would not contribute to the total length in subsequent analysis. A degree of manual editing was performed for each cell, such that any branch without a discernible thickness was removed from the network object. The widths of network branches were also calculated with the aid of the MATLAB GUI, which allows the user to add and adjust width measurements across a given edge. For longer edges, one measurement point close to the branching point and the other closer to the end of the edge are chosen. Total subtree length, volume, depth, and bushiness following each branch was calculated using MATLAB written code. Volume was measured using the diameter and length of each edge bounded between two nodes. Bushiness is defined as the total subtree length (L) over the subtree depth (D), where D is the path length from the base of the subtree to each distal tip, weighted by the length of each subtree. Proportional scaling of sister subtrees (V ~ L and r^2~L/D, Figures 6I and 6J) was assessed by measuring each sister subtree pair (ST1 and ST2, where ST1 and ST2 are the length, volume, truck thickness (r^2), or bushiness (L/D) for sister subtree 1 and 2), calculating asymmetry between the sisters for each metric according to ST1-ST2)/(ST1+ST2), and then comparing asymmetries for volume versus length and for trunk thickness versus bushiness. Equivalent asymmetries indicate proportional scaling of the metrics (e.g., $V_{asym} = L_{asym}$ indicates $V_1/V_2 = L_1/L_2$, or equivalently V ~ L for the sister subtrees). Note that proportionality does not hold when comparing non-sister subtrees (e.g., comparing subtrees from different levels in the tree), and calculating asymmetries allows for normalization of metrics for sister subtrees, enabling statistical comparisons across multiple entire trees.

Mathematical modeling

Mean-field models for mitochondrial distributions in a dendritic tree

Comparing average subtree densities in models with uniform transport. We first consider models where the mitochondrial transport parameters are spatially uniform (constant velocity v and stopping rate k_s throughout the arbor, $\beta = 0$). Steady state linear densities of motile mitochondria ($\rho_i^{\pm}$) and stationary mitochondria (ρ_i^s) are defined by Equation 1 in the main text. These densities are constant on individual branches, with values set by boundary conditions at the junction, which require incoming flux to equal outgoing flux at steady-state. Namely, the solutions to Equation 1 are given by:

$$\rho_i^+ = \rho_i^-, \qquad \text{(Equation 2a)}$$

$$\rho_i^s = \frac{k_s}{k_w}\rho_i^w, \qquad \text{(Equation 2b)}$$

$$\rho_1^+ = \frac{\psi\rho_0^+}{1+\psi}, \rho_2^+ = \frac{\rho_0^+}{1+\psi} \qquad \text{(Equation 2c)}$$

where $\rho_i^w = \rho_i^+ + \rho_i^-$ is the linear density of motile mitochondria on branch i, and ρ_0^+, ρ_1^+, ρ_2^+ are linear densities of anterograde mitochondria in a mother branch and its two daughter branches respectively. The junction-specific parameter $\psi = \rho_1^+/\rho_2^+$ determines how the anterograde flux splits at the junction. In this manuscript we consider both the simple model of equal splitting $\psi = 1$ as well as the model where anterograde mitochondria split in proportion to daughter branch area ($\psi = r_1^2/r_2^2$, supported by experimental data). The volume densities in the daughter branches can be expressed as:

$$c_1 = \left(\frac{\psi c_0}{1+\psi}\right)\frac{r_0^2}{r_1^2},\quad c_2 = \left(\frac{c_0}{1+\psi}\right)\frac{r_0^2}{r_2^2} \qquad \text{(Equation 3)}$$

where the relationship holds for both the motile and stationary mitochondria densities (if stopping rate k_s is assumed constant on all branches, $\beta = 0$).

A particularly simple version of the model is one where anterograde mitochondria split equally at all junctions ($\psi = 1$). Then the volume density a branch that is *i* junctions below the trunk is given by:

$$c_i = \left(\frac{1}{2^i}\right)\left(\frac{r_{trunk}^2}{r_i^2}\right)c_{trunk} \qquad \text{(Equation 4)}$$

If we further assume that sister branch widths are split equally at all junctions ($\mu = r_1/r_2 = 1$), this implies that two sister branches will always have equal volume densities. In this case, we can express the branch radii according to $r_i = r_{trunk}/2^{i/\alpha}$, where α describes the parent-daughter scaling relationship, with $r_0^\alpha = r_1^\alpha + r_2^\alpha$ relating the parent branch width r_0 and daughter branch widths r_1, r_2 at each junction. The volume density in a branch separated by *i* junctions from the trunk is then:

$$c_i = 2^{(2/\alpha-1)i}c_{trunk} \qquad \text{(Equation 5)}$$

If the arbor obeys Da Vinci scaling ($\alpha = 2$), which conserves cross-sectional area across junctions, then the volume density of mitochondria must be equal in all branches of the tree. Thus, there is no distal enrichment and perfectly symmetric mitochondrial distributions. By contrast, in a tree where $\alpha < 2$ (as for Rall's Law, $\alpha = 3/2$), the volume density will increase as a power law with the number of junctions away from the trunk. Similarly, for trees with $\alpha > 2$ (as for Murray's Law, $\alpha = 3$), the volume density will decrease as a power law toward more distal branches.

Alternately, we consider the case where the anterograde flux at each junction splits in proportion to the daughter branch area: $\psi = r_1^2/r_2^2$. From Equation 2, this gives the following relation between parent and daughter volume densities:

$$c_1 = c_2 = \frac{c_0 r_0^2}{r_1^2+r_2^2} \qquad \text{(Equation 6)}$$

In all cases, the volume density in two sister branches must be equal. If the arbor obeys Da Vinci scaling ($\alpha = 2$), then the volume density will be constant throughout the tree (i.e., the average volume density in all sister subtree pairs will be equal). However, for non-Da Vinci-scaled arbors with asymmetric branching patterns and unequal sister-branch radii, the average volume densities in two sister subtrees may be quite different.

As an example, we consider specifically the mitochondrial volume density in arbors that obey Rall's Law relating parent and daughter branch widths ($r_0^a = r_1^\alpha + r_2^\alpha$, with $\alpha = 3/2$). Assuming uniform mitochondrial transport ($\beta = 0$) and anterograde splitting in proportion to branch area ($\psi = r_1^2/r_2^2$), we show that mitochondrial densities increase with distance from the soma and that asymmetric sister subtrees must in general have unequal average densities. The relationships below apply to both motile and stationary mitochondrial densities.

We begin by focusing on a single junction with a parent trunk of radius r_0 and linear mitochondrial density ρ_0, and daughter trunk radii r_1, r_2 and linear densities ρ_1, ρ_2. A single (junction-dependent) parameter, $\mu = r_1/r_2$, describes how the dendritic width is split between sister branches. For convenience, we define a related quantity: $\widehat{\mu}_0 = r_1^\alpha/r_0^\alpha = \mu^\alpha/(1+\mu^\alpha)$ which describes how the first sister branch radius compares to that of the parent branch. The ratio of mitochondrial volume density between the daughter branches and the parent can be written as:

$$\frac{c_1}{c_0} = \frac{c_2}{c_0} = \frac{r_0^2}{r_1^2+r_2^2} = \frac{1}{\widehat{\mu}_0^{2/\alpha}+(1-\widehat{\mu}_0)^{2/\alpha}} \qquad \text{(Equation 7)}$$

For $\alpha < 2$, this ratio is always above unity ($c_1/c_0 > 1$), except in the edge cases of $\mu_0 = 1$ or $\mu_0 = 0$, which would correspond to one daughter branch disappearing. Thus, the volume density of mitochondria in the daughter branches of a Rall's Law tree is always higher than in the parent branch. This is a direct consequence of the reduced cross-sectional area in the daughter branches.

We next consider whether it is possible to choose values of the sister trunk splitting parameter μ_i at each junction *i* in a way that ensures equitable mitochondrial distribution in the two sister subtrees. We begin by defining two parameters for a subtree initiating from trunk 0. First, we define the parameter η_0, which relates the total volume of the subtree to the cross-sectional area of the trunk: $V_0 = \eta_0 r_0^2$. For a symmetric Da Vinci tree, where total cross-sectional area is conserved at each junction, the parameter η_0 represents the depth of the tree (distance from soma to distal tips). For a symmetric Rall's Law tree, however, the value of η_0 is less than the depth, due to the narrowing of total cross-sectional area below each junction. Second, we define the parameter z_0, which relates the average volume density of mitochondria within the subtree to the density within the trunk: $\langle c\rangle_0 = z_0\rho_0/r_0^2$. For a Da Vinci tree, under the assumption of uniform mitochondrial transport, $z = 1$ for all junctions regardless of the tree morphology. For a Rall's law tree with at least one junction, the increase in density from parent to daughter branches implies that $z_0 > 1$. These two parameters describing the volume and average mitochondrial density in a subtree, can be expressed recursively:

$$\eta_0 = l_0 + \eta_1 \widehat{\mu}_0^{2/\alpha} + \eta_2 (1 - \widehat{\mu}_0)^{2/\alpha} \quad \text{(Equation 8a)}$$

$$z_0 = \frac{l_0 + \frac{z_1 \widehat{\mu}_0^{2/\alpha} + z_2 (1 - \widehat{\mu}_0)^{2/\alpha}}{\widehat{\mu}_0^{2/\alpha} + (1 - \widehat{\mu}_0)^{2/\alpha}}}{l_0 + \eta_1 \widehat{\mu}_0^{2/\alpha} + \eta_2 (1 - \widehat{\mu}_0)^{2/\alpha}} \quad \text{(Equation 8b)}$$

where η_0, z_0 are the values for a tree with parent trunk 0 and $\eta_{1,2}$, $z_{1,2}$ are values for the daughter subtrees with trunks 1 and 2.

For two sister subtrees, the volume densities in the trunk must be the same (Equation 6). Consequently, the subtrees will have equal average mitochondrial densities if and only if $z_1 = z_2$. If we want to establish a universal rule for splitting sister trunks (i.e., defining μ_i values at each junction) that depends only on the morphology of the downstream subtree, then the only way to ensure equitable mitochondrial densities throughout all sister subtrees in the arbor would be for all values of z_i to be set to a single constant $z_i = z^*$. For a Rall's Law arbor, we would need to pick a value $z^* > 1$ when setting such a rule. In Figure S5, we consider a Rall-scaled arbor with junction connectivities and branch lengths extracted from a *Drosophila* HS arbor skeleton. Starting from the distal branches of the tree, we recursively solve, where possible, for the value of μ_i at each junction that would set $z_i = z^*$ for the parent trunk leading to that junction. Where a solution is impossible (always due to the maximum value of z_i being below z^*), we pick the splitting that maximizes z_i. Red circles in the figure show junctions where a solution was not found that could enable the two sister subtrees to have equal mitochondrial densities. Choosing a high value of z^* makes it impossible to enforce equitable mitochondrial densities in many pairs of sister subtrees (Figure S5A), in contrast to experimental observations. On the other hand, choosing $z^* \approx 1$ leads to an unrealistic collapse of the arbor to a single primary path in order to maintain equitable mitochondrial distribution (Figure S5B). Overall, these calculations imply that a Rall's tree morphology (together with uniform mitochondrial transport kinetics and anterograde flux splitting in proportion to trunk area) leads to increased mitochondrial densities in distal branches but cannot allow for a realistic splitting of branch widths that establishes equal mitochondrial densities between sister subtrees.

Subtree densities in a Da Vinci tree with non-uniform transport. Rather than assuming spatially constant mitochondrial motility, an alternative model can be constructed where mitochondria are more likely to halt on narrower branches, with stopping rate $k_s \sim 1/r_i^{\beta}$, while the restarting rate k_w and pause-free velocities v remain constant. It should be noted that the steady-state densities (Equation 1) depend only on the ratio of k_s/k_w in each branch and not on the rates themselves. Thus, equivalent model results would be obtained if the restarting rate k_w was instead made to vary with branch width.

One simple model for width-dependent stopping would be to set the rate inversely proportional to the cross-sectional area of each branch: $k_{s,i} = k_s^*/r_i^2$, corresponding to $\beta = 2$. With $k_s \sim 1/r^2$, the linear density of stationary mitochondria in branch i is given by:

$$\rho_i^{(s)} = \frac{k_s^*}{k_w} \rho_i^{(w)} \Big/ r_i^2 \quad \text{(Equation 9)}$$

where $\rho_i^{(w)} = \rho_i^+ + \rho_i^-$ is the motile linear density of mitochondria. At a junction with daughter branches 1 and 2, we assume this motile linear density splits according to $\psi = \rho_1^+/\rho_2^+ = r_1^2/r_2^2$, in keeping with experimental measurements (Figure 5).

In a tree with Da Vinci scaling, the volume density of motile mitochondria is spatially constant, so that all branches have $c_i^{(w)} = c_{trunk}^{(w)} = \rho_{trunk}^{(w)}/r_{trunk}^2$. We can then calculate the average volume density of the stationary population in a subtree with total volume V_{ST} and total branch length L_{ST}:

$$\langle c^{(s)} \rangle_{ST} = \frac{\sum_{i \in ST} \rho_i^{(s)} l_i}{\sum_{i \in ST} r_i^2 l_i} = \frac{\frac{k_s^*}{k_w} c_{trunk}^{(w)} \sum_i l_i}{V_{ST}} \sim \frac{L_{ST}}{V_{ST}} \quad \text{(Equation 10)}$$

where the summations are over all branches in the subtree. Therefore, the ratio between the average stopped mitochondrial densities in sister subtrees becomes:

$$\frac{\langle c^{(s)} \rangle_1}{\langle c^{(s)} \rangle_2} = \frac{L_1/V_1}{L_2/V_2} \quad \text{(Equation 11)}$$

Keeping in mind that $\langle c \rangle = \langle c^{(w)} \rangle + \langle c^{(s)} \rangle$ and that $c^{(w)}$ is the same for all branches in a Da Vinci tree, we see that equitable distribution of mitochondria between sister subtrees can be achieved only if the volume of each sister subtree is proportional to its total length:

$$\frac{L_1}{V_1} = \frac{L_2}{V_2} \quad \text{(Equation 12)}$$

For a Da Vinci arbor, this proportional scaling of sister subtree length and volume can be achieved via a particular form for the sister trunk width relation ($\mu = r_1/r_2$). We begin by defining the depth of a tree, D, via a recursive approach. For a subtree consisting of a single branch of length l_1, the depth is simply defined as that branch length ($D_1 = l_1$). Next, we consider a tree with trunk of index 0, splitting at a downstream junction between subtree trunks 1 and 2. We define the depth of the tree according to the following formula:

$$D_0 = l_0 + \frac{L_1+L_2}{L_1/D_1+L_2/D_2} \quad \text{(Equation 13)}$$

where D_1, D_2 are the depths and L_1, L_2 are the total branch lengths of the subtrees starting with branch 1 and 2, respectively. Conceptually, this expression averages the inverse depths of the two subtrees, weighted by their respective lengths, and adds on the length of the parent trunk. We note that in the case where the two subtrees have the same depth ($D_1 = D_2$) then the overall depth of the tree becomes $D_0 = l_0 + D_1$. Thus, in an arbor where all distal tips are the same distance from the parent node, the depth of the tree will simply be equal to that distance.

We now consider the specific case of a Da Vinci arbor that additionally obeys the criterion in Equation 12, where the volume of a sister subtree is proportional to its total length. As before, we express the volume of the arbor in terms of the prefactor η_0 according to $V = \eta_0 r_0^2$. We then show by induction that under these assumptions the prefactor is equal to the depth: $D_0 = \eta_0$. First, we use the length-volume proportionality to express the volume of each subtree in terms of the parent volume and the subtree lengths according to:

$$V_0 = l_0 r_0^2 + V_1 + V_2 \quad \text{(Equation 14a)}$$

$$V_1 = \frac{L_i}{L_1+L_2}(V_1 + V_2) = \frac{L_i}{L_1+L_2}\left(V_0 - l_0 r_0^2\right) = \eta_i r_i^2 \quad i = 1,2 \quad \text{(Equation 14b)}$$

Next, we can apply the Da Vinci law relating parent and daughter branch widths:

$$r_0^2 = r_1^2 + r_2^2 = \frac{L_1/\eta_1+L_2/\eta_2}{L_1+L_2}\left(V_0 - l_0 r_0^2\right), \quad \text{(Equation 15a)}$$

$$V_0 = \left(l_0 + \frac{L_1+L_2}{L_1/\eta_1+L_2/\eta_2}\right) r_0^2 = \eta_0 r_0^2 \quad \text{(Equation 15b)}$$

Thus, we see that if the two subtrees have depths $D_1 = \eta_1$ and $D_2 = \eta_2$, then the overall tree will also have $D_0 = \eta_0$, where depth is defined according to Equation 12. Since single branches have $D_i = \eta_i$ by definition, this argument implies that all trees obeying Da Vinci scaling and length-volume proportionality have volume given by $V_0 = D_0 r_0^2$.

Finally, we note that, for a Da Vinci tree, the proportionally of length and volume can now be translated directly into a relationship between sister subtree trunk widths:

$$\frac{L_1/V_1}{L_2/V_2} = \frac{L_1/(D_1 r_1^2)}{L_2/(D_2 r_2^2)} = 1 \quad \text{(Equation 16a)}$$

$$\mu^2 = \frac{r_1^2}{r_2^2} = \frac{L_1/D_1}{L_2/D_2} = \frac{b_1}{b_2} \quad \text{(Equation 16b)}$$

where we define the 'bushiness' of a subtree (b_i) as its total length divided by its depth: $b_i = L_i/D_i$. Trees with high bushiness are broader, in the sense of having a greater total length of branches at a given depth, arising from more frequent junctions (Figure 4B).

Overall, we have shown that in an arbor obeying the Da Vinci rule ($\alpha = 2$), where mitochondrial stopping is inversely proportional to branch area ($\beta = 2$), equal densities of mitochondria between sister subtrees will be obtained if the sister trunk cross-sectional areas are split in proportion to the subtree bushiness (Equation 15b).

Average subtree densities for general transport behavior in Da Vinci arbors. We next consider a generalization of the mitochondrial distribution model to the case where both the stopping rate $k_{s,i}$ and the pause-free velocity v_i can vary depending on the branch width. At steady state, the conservation of incoming and outgoing flux into a branch junction gives a relationship between the motile mitochondria density $\rho_0^{(w)}$ in the parent trunk and the daughter branches. We maintain the assumption that the splitting of mitochondrial flux into each daughter branch is proportional to the cross-sectional area. Specifically, this gives the two conditions:

$$v_0 \rho_0^{(w)} = v_1 \rho_1^{(w)} + v_2 \rho_2^{(w)} \quad \text{(Equation 17a)}$$

$$\psi = \frac{v_1 \rho_1^{(w)}}{v_2 \rho_2^{(w)}} = \frac{r_1^2}{r_2^2} \quad \text{(Equation 17b)}$$

where we note that $\rho^{(w)} = 2\rho^+$ by symmetry. The density of stationary mitochondria in each branch is given by $\rho_i^{(s)} = \frac{k_{s,i}}{k_w}\rho_i^{(w)}$.

Assuming a Da Vinci relationship between parent and daughter branch widths, we can solve for the volume density of mitochondria in daughter branches as follows:

$$v_0\rho_0^{(w)} = v_1\rho_1^{(w)}\left(1+\frac{r_2^2}{r_1^2}\right) = \frac{v_1\rho_1^{(w)}r_0^2}{r_1^2} \quad \text{(Equation 18a)}$$

$$c_1^{(w)} = \rho_1 \Big/ r_1^2 = c_0^{(w)}\frac{v_0}{v_1} \quad \text{(Equation 18b)}$$

Consequently, throughout the entire arbor, the motile volume density in each branch can be written in terms of the local velocity and the density in the parent trunk of the full tree: $c_i^{(w)} = c_{trunk}^{(w)}\frac{v_{trunk}}{v_i}$. The total volume density on a branch, including motile and stationary mitochondria, can be expressed in terms of the average velocity (with pauses included), given by $\overline{v}_i = \frac{k_w}{k_w+k_{s,i}}v_i$. Specifically:

$$c_i = c_i^{(w)} + c_i^{(s)} = \left(\frac{k_{s,i}+k_w}{k_w}\right)c_{trunk}^{(w)}\frac{v_{trunk}}{v_i} = c_{trunk}^{(w)}v_{trunk} \Big/ \overline{v}_i \quad \text{(Equation 19)}$$

The average volume density of mitochondria in a subtree is then given by:

$$\langle c\rangle_{ST} = \frac{\sum_{i\in ST}c_i^{(w)}r_i^2l_i}{\sum_{i\in ST}r_i^2l_i} = \frac{1}{V_{ST}}\sum\nolimits_{i\in ST}\frac{r_i^2l_ic_{trunk}^{(w)}v_{trunk}}{\overline{v}_i} = c_{trunk}^{(w)}v_{trunk}\langle 1/\overline{v}\rangle_V \quad \text{(Equation 20)}$$

where the final term denotes the volume-weighted average of the inverse velocity over the subtree: $\langle 1/\overline{v}\rangle_V = \left(\sum_{i\in ST}r_i^2l_i(1/\overline{v}_i)\right)/V_{ST}$.

We consider the case where the average velocity (including pauses) along a branch scales as a power law of the branch width: $\overline{v}_i \sim r_i^{\gamma}$. Under this assumption, the ratio of sister subtree densities is given by:

$$\frac{\langle c\rangle_1}{\langle c\rangle_2} = \frac{\langle 1/\overline{v}\rangle_{V_1}}{\langle 1/\overline{v}\rangle_{V_2}} = \frac{V_2}{V_1}\frac{\sum_{i\in ST_1}r_i^{2-\gamma}l_i}{\sum_{i\in ST_2}r_i^{2-\gamma}l_i} \quad \text{(Equation 21)}$$

In the case that $\gamma = 2$, this relationship reduces to $\langle c\rangle_1/\langle c\rangle_2 = (L_1/V_1)/(L_2/V_2)$, and equal densities of mitochondria between sister subtrees are again achieved when the subtree volume is proportional to its total length. A particular case that leads to $\gamma = 2$ is where restarting rates are low ($k_{s,i} \gg k_w$ throughout most of the tree), pause-free velocities are constant, and the stopping rate scales inversely with cross-sectional area ($k_{s,i} \sim 1/r_i^2$). This is the simplified case considered in the main text.

Mitochondrial processivity. Our basic model (Equation 1 in the main text) assumes that mitochondria lose all memory of their direction of motion when they stop. Processive motion that persists beyond individual stopping events can be incorporated in a more general model with different stopped states (ρ_i^{s+}, ρ_i^{s-}) that retain a memory of prior direction of motion, and a switching probability p_s for the organelle to reverse direction upon restarting. The steady-state equations then generalize to:

$$\frac{d\rho_i^+}{dt} = -v\frac{d\rho_i^+}{dx} - k_{s,i}\rho_i^+ + k_{w,i}p_s\rho_i^{s-} + k_{w,i}(1-p_s)\rho_i^{s+} = 0 \quad \text{(Equation 22a)}$$

$$\frac{d\rho_i^-}{dt} = v\frac{d\rho_i^-}{dx} - k_{s,i}\rho_i^- + k_{w,i}p_s\rho_i^{s+} + k_{w,i}(1-p_s)\rho_i^{s-} = 0 \quad \text{(Equation 22b)}$$

$$\frac{d\rho_i^{s+}}{dt} = k_{s,i}\rho_i^+ - k_{w,i}\rho_i^{s+} = 0 \quad \text{(Equation 22c)}$$

$$\frac{d\rho_i^{s-}}{dt} = k_{s,i}\rho_i^- - k_{w,i}\rho_i^{s-} = 0 \quad \text{(Equation 22d)}$$

These equations reduce to the base model with $p_s = 1/2$, with the total density of stopped mitochondria defined as $\rho_i^s = \rho_i^{s+} + \rho_i^{s-}$.

The solutions to this set of equations can be found by matching boundary conditions at the dendritic tips and branch points. As the base model described in the main text, reflecting boundaries at the tips and conservation of mass as the junction impy that $\rho_i^+ = \rho_i^-$ at all boundaries. This relationship, together with Equation 22, leads to steady-state solutions that constant along each individual branch, with $\rho_i^{s\pm} = (k_{s,i}/k_{w,i})\rho^{\pm}$ everywhere. Finally, adding Equations 22c and 22d together to set the total density of stopped mitochondrial reduces this model back to Equation 1.

Similarly, we can reduce mitochondrial processivity by introducing a new rate $k_{r,i}$ for reversing the direction of motion while remaining in the motile state. In this case, the steady-state equations become:

$$\frac{d\rho_i^+}{dt} = -v\frac{d\rho_i^+}{dx} - k_{s,i}\rho_i^+ + \frac{1}{2}k_{w,i}\rho_i^s + k_{r,i}\rho_i^- - k_{r,i}\rho_i^+ = 0 \quad \text{(Equation 23a)}$$

$$\frac{d\rho_i^-}{dt} = v\frac{d\rho_i^-}{dx} - k_{s,i}\rho_i^- + \frac{1}{2}k_{w,i}\rho_i^s + k_{r,i}\rho_i^+ - k_{r,i}\rho_i^- = 0 \quad \text{(Equation 23b)}$$

$$\frac{d\rho_i^s}{dt} = k_{s,i}\left(\rho_i^+ + \rho_i^-\right) - k_{w,i}\rho_i^s = 0 \quad \text{(Equation 23c)}$$

As in the base model, solving these equations (with reflecting conditions at the tips) implies that $\rho_i^+ = \rho_i^-$ at all boundaries, and the terms involving the reversal rate thus disappear, reducing the system back to Equation 1 in the main text.

Overall, the processivity of mitochondrial motion in a dendritic tree has no effect on the steady-state distribution of mitochondrial mass.

Generation of model dendrite skeletons

Dendrite skeletons with well-defined branch lengths and connectivity were obtained either from MCFO images of *Drosophila* HS neurons as described above, from published swc files,[46] from HS skeletons traced through a ssTEM dataset,[48] or from synthetically constructed trees. The synthetic trees were constructed in Python 3.7.6 using the NetworkX library. The skeleton of a binary tree was initiated with a single junction consisting of a parent branch and two daughter branches of unit length. Moving downstream along the tree, each daughter branch either terminated as a distal tip (with probability $^1/_3$), increased in length by an additional unit (probability $^1/_3$), or branched into two more daughter branches (probability $^1/_3$). This process was repeated up to a preset maximum path distance (40 unit branch lengths) from the arbor parent node to the distal tips. Examples of the resulting random-topology binary tree structures are shown in Figure S3A.

Quantification of mitochondrial distribution patterns in model dendrites

For each dendrite skeleton, the radius of the primary branch (the trunk of dendritic arbor) was set to $r_0 = 1$ (in dimensionless units). The radii of the rest of the branches in the arbor were set based on two morphological scaling rules (parent-daughter scaling and sister-sister scaling). Mitochondrial linear densities within each branch were determined by analytical solutions of the linear differential equations for all combinations of the morphological and transport scaling parameters (α, μ, β, and ψ), as described in the main text. Model predictions of mitochondrial localization patterns were quantified using two parameters: distal mitochondrial enrichment (δ) and average asymmetry across sister subtrees (ζ). Distal mitochondrial enrichment was calculated according to $\delta = \frac{\langle c^s_{distal}\rangle}{\langle c^s_{primary}\rangle}$, where $\langle c^s_{distal}\rangle$ and $\langle c^s_{primary}\rangle$ are the average volume densities of stationary mitochondria in the distal and primary dendrites, respectively, and distal dendrites were defined as those whose distance from the soma is greater than 75% the maximum value in the tree. The asymmetry metric was calculated as the root-mean-squared asymmetry in volume densities of stationary mitochondria in sister subtrees ($\langle c^s\rangle_1$ and $\langle c^s\rangle_2$): $\zeta = \sqrt{\frac{1}{N_b}\sum_b\left(\frac{\langle c^s\rangle_1 - \langle c^s\rangle_2}{\langle c^s\rangle_1 + \langle c^s\rangle_2}\right)^2}$, where the index b enumerates the junctions, N_b is the total number of junctions in the arbor, and $\langle c^s\rangle_{1/2}$ is the total volume density of stationary mitochondria is daughter subtree 1 and 2, respectively, from each junction. All model calculations were carried out using custom written MATLAB code.

QUANTIFICATION AND STATISTICAL ANALYSIS

Statistical parameters and significance are indicated in the legends of each figure, including the definitions of error bars and the number of samples. Statistical significance was determined by t-tests (based on the assumption that all data was normally distributed), and $p < 0.05$ was considered statistically significant. Unless otherwise indicated, data was collected from one neuron per fly.